ANALYSIS OF AN AIRFOIL WITH ROTATING CYLINDER

FOR IMPROVED PERFORMANCE

by

Anfal Al-Abdullah

A Thesis presented to the Faculty of the
American University of Sharjah
College of Engineering
In Partial Fulfillment
of the Requirements
for the Degree of

Master of Science in
Mechanical Engineering

Sharjah, United Arab Emirates

April 2019

Approval Signatures

We, the undersigned, approve the Master's Thesis of Anfal Al-Abdullah

Thesis Title: Analysis of an Airfoil with Rotating Cylinder for Improved Performance.

Signature	**Date of Signature** (dd/mm/yyyy)

_____   _____

Dr. Mohammad Omar Hamdan
Associate Professor, Department of Mechanical Engineering
Thesis Advisor

_____   _____

Dr. Muhammad Imran Qureshi
Assistant Professor of Mechanical Engineering
Thesis Co-Advisor

_____   _____

Dr. Rachid Chebbi
Professor, Department of Chemical Engineering
Thesis Committee Member

_____   _____

Dr. Bassam Abu-Nabah
Assistant Professor, Department of Mechanical Engineering
Thesis Committee Member

_____   _____

Dr. Mamoun Abdel-Hafez
Head, Department of Mechanical Engineering

_____   _____

Dr. Lotfi Romdhane
Associate Dean for Graduate Affairs and Research
College of Engineering

_____   _____

Dr. Naif Darwish
Acting dean, College of Engineering

_____   _____

Dr. Mohamed El-Tarhuni
Vice Provost for Graduate Studies

Acknowledgement

My immense gratitude extends towards Dr. Muhammad Imran Qureshi, with whom this research work was started and its biggest chunk was executed. I cannot thank him enough for the dedication, patience, and support he has provided throughout the duration of this study.

A sincere appreciation is reserved to Dr. Mohammad Hamdan, for kindly welcoming this research, despite being in its final stages, and providing the generous guidance and assistance that have eventually allowed this research to be concluded.

I would also like to thank the thesis committee members, Dr. Rachid Chebbi and Dr. Bassam Abu-Nabah, whom it has been a privilege to have the thesis examined by them. Their valuable feedback has certainly aided in further improving this work.

No words would be sufficient to thank my beloved father, mother and sister. They have wholeheartedly never ceased to support and hearten me throughout my lifelong journey of education, and I am eternally grateful for them. I am fortunate to have the most wonderful friend, Rahma Jubran, who has been by my side throughout all the ups and downs, urging me to invest in the most of my capabilities. Special thanks to Hanin Atwani, for being the best friend and colleague I could ever ask for, with whom I could truly work in harmony. I am thankful as well to Sara Yaseen, Omnia Sarsar, Mariam El-Shazly, Amritha Falgunan, Ms. Maha Shushaa, Eng. Rami Shunnag, and every friend, acquaintance, and colleague who took the time to ask how my work was going and cheered for me throughout this ride.

Last but not least, I am quite grateful to the American University of Sharjah, specifically the Mechanical Engineering department, for sponsoring my studies while granting me a hands-on experience in the academic field work.

Dedication

To my beloved father, for unceasingly believing in the best of my potential,

And my cherished mother, for immersing me with the warmest compassion…

Abstract

Among the multiple techniques used for boundary-layer control and flow separation delay, moving surface boundary-layer control is one of the promising approaches. Adding a rotating cylinder is one means of enhancing the aerodynamic performance of an airfoil, given that it serves to be an effective way in delaying stall. In this study, a rotating cylinder has been embedded in the leading edge of a NACA0024 airfoil. The wing model has been analyzed experimentally as well as numerically. The airfoil has been tested experimentally in a subsonic wind tunnel under different angles of attack, α, and cylinder-to-freestream velocity ratios, ζ. The effect of both parameters on the aerodynamic performance has been investigated, mainly through calculation of the lift coefficient, C_L, the drag coefficient, C_D, lift-to-drag ratio, C_L/C_D, and stall angle of attack, α_{stall}. Additionally, flow visualization has been carried out to get a perspective on the behavior of the rotating cylinder. Multiple photos have been captured where the streamlines of the flow are clear to the eye. A 2D numerical simulation using Computational Fluid Dynamics (CFD) has been carried out using ANSYS FLUENT 17.0 software. Through replicating the exact conditions of the experimental work, the CFD simulation has been successfully validated by its experimental counterpart. Results have shown a promising increase in the maximum lift coefficient from 0.98 at $\zeta = 0$ to 1.45 at $\zeta = 6$, which translates to around a 48% increase. The corresponding stall angle of attack has increased simultaneously from $\alpha = 15°$ at $\zeta = 0$, to around $\alpha = 35°$ at $\zeta = 6$. This increase of lift, however, is accompanied by a 47% increase in maximum drag coefficient. Furthermore, varying the cylinder exposure between 20% and 40% has shown an increase of 6.6% to 19.6% in the lift coefficient at $\alpha = 10°$ and 20°, respectively.

Keywords: *Boundary layer control; Active flow control; Stall delay; Rotating cylinder; Computational fluid dynamics; Turbulence; NACA0024.*

Table of Contents

List of Figures

List of Tables

Nomenclature

c	Airfoil chord length (m)
C_A	Coefficient of axial force acting on the airfoil surface
C_D	Drag coefficient
c_f	Skin friction coefficient
C_L	Lift coefficient
C_L/C_D	Lift-to-drag ratio
C_N	Coefficient of normal force acting on the airfoil surface
c_P	Pressure coefficient
P	Tap pressure (Pa)
$P_{D,\infty}$	Freestream dynamic pressure (Pa)
$P_{S,\infty}$	Freestream static pressure (Pa)
t	The maximum thickness of the airfoil (m)
U_c	Cylinder tangential speed (m/s)
U_∞	Freestream velocity of the flow (m/s)
x	Horizontal chord distance measured from the leading edge (m)
x/c	Non-dimensional chord horizontal distance measured from the leading edge
y	Vertical distance measured from the surface of the airfoil (m)

Abbreviations

2D	Two Dimensional
3D	Three Dimensional
CFD	Computational Fluid Dynamics
SST	Shear Stress Transport

Greek Letters

α Angle of attack (°)

α_{stall} Stall angle of attack (°)

μ Air dynamic viscosity (Pa.s)

ρ Air density (kg/m^3)

ζ Cylinder-to-freestream velocity ratio, U_c/U_∞

Non-dimensional Numbers

Re Reynolds Number

Subscripts

c Cylinder

l Lower airfoil surface

u Upper airfoil surface

∞ Freestream

Chapter 1. Introduction

This chapter presents an overview of the thesis. It introduces the objectives, key findings and contributions, and subsequently provides a short summary on the contents of the thesis in an organized manner.

1.1. Overview

Researchers in the field of aerodynamics are constantly seeking to improve the aerodynamic performance of airfoils, and boundary-layer control is considered of utmost importance when it comes to this objective [1]. Under ordinary conditions, flow separation occurs on the upper surface of an airfoil. This creates vortices and reversed flow, which in turn stimulate a loss of lift and a likely increase in drag. The lift coefficient increases with increased angle of attack, α, yet this increase is not indefinite; there is a maximum attainable value of lift coefficient, after which increasing the angle of attack triggers a drop in it. When this occurs, the airfoil is said to be stalled, and the corresponding angle at such case is called the critical angle of attack, or stall angle of attack α_{stall} [2]. Stall is an issue of a grand concern at higher angles of attack, since it brings about an abrupt decrease in lift. Therefore, it ought to be avoided at all costs.

Stall, however, can be delayed by employing several boundary-layer control techniques. Adding a rotating cylinder at the leading edge of an airfoil is among those techniques. It aids in delaying flow separation, since the rotation of the cylinder decreases the relative motion between the airfoil surface and freestream velocity, which hinders the initial growth of the boundary layer. The rotating cylinder essentially serves in adding extra momentum to the flow, which increases the velocity of the flow at the airfoil's upper surface. And thus, its advantages lie in keeping the flow attached to the airfoil at higher angles of attack, which in turn increases the stall angle of attack, corresponding to a higher lift coefficient.

1.2. Thesis Objectives

The primary focus of this thesis is to control the boundary layer on the upper surface of a NACA0024 airfoil using a rotating cylinder embedded at its leading edge. The main objective of this is to improve the airfoil's aerodynamic performance, i.e. increasing lift and lift-to-drag ratio, and delaying flow separation, which would result in a higher stall angle of attack. This is done through an experimental analysis followed

up by a numerical simulation one using Computational Fluid Dynamics (CFD). Experimental data are first obtained through conducting tests on a prepared NACA0024 airfoil wing model with a leading-edge rotating cylinder in the Aeronautics lab at the American University of Sharjah. The data obtained through experiments are then used as a validation reference when conducting the CFD simulation in ANSYS FLUENT 17.0 software. After validating the CFD model, further numerical parametric studies are carried out to better quantify the benefits of a rotating cylinder.

1.3.   Research Contribution

The validated CFD model is used as a replacement for the actual setup in order to conduct further studies that would not be easily achieved in reality due experimental and economic limitations. The key findings and contributions of this research can be summarized in the following:

- The effect of increasing the rotational speed of the cylinder and the cylinder-to-freestream velocity ratio, ζ, on the aerodynamic performance in terms of lift and drag coefficients are studied for cases of $\zeta = 0, 1, 2, 4$ and 6, thus going beyond the experimental limits of $\zeta = 0, 1$ and 2. It has been found and proven that increasing ζ results in a higher lift coefficient at a given incidence with a simultaneous increase in drag coefficient. It has also been found that increasing ζ aids in delaying flow separation to higher angles of attack, which in turn brings about an increased stall angle of attack α_{stall}.

- The effect of changing the percentage of cylinder exposure on the aerodynamic performance is studied as well, by trying different symmetrical exposure values from 20%, 30% and 40%, in contrast to the experimental non-symmetric exposure value of 25.5%. Increasing the aforementioned exposure of the rotating cylinder has been found to result in an increase in lift coefficient as well as drag coefficient. The amount of increase, however, is inconsistent; increasing the exposure at higher α has resulted in a higher rate of increase in lift-to-drag ratio in comparison to lower α.

1.4.   Thesis Organization

This thesis presents a comprehensive experimental and numerical study of a NACA0024 airfoil with a leading-edge rotating cylinder. The experimental data are used as a basis for validating the numerical simulation. After the simulation is validated,

data are obtained for higher cylinder-to-freestream velocity ratios. Finally, a study on the effect of variation cylinder exposure on the aerodynamic performance is conducted.

Chapter 2 of this thesis sheds a light on the background theory of flow separation, airfoil stalling and proposed boundary layer control techniques. It as well presents the related research works available in literature and their latest findings.

Chapter 3 discusses the experimental setup in depth in terms of equipment, conditions, and limitations. It also covers the theoretical formulation used in data analysis, including calculation of pressure, skin friction, lift and drag coefficients. Finally, it presents a summary of the experimental results.

As for the following Chapter 4, it introduces the methodology followed in the numerical simulation, including the geometry, mesh, turbulence model and boundary conditions, in addition to mesh-independence analysis and turbulence models comparison. The chapter then discusses the two numerical studies conducted, variation of cylinder-to-freestream ratio and variation of the cylinder exposure and their effect on the aerodynamic performance. Chapter 5 comprises of the results and discussion, covered in-depth, of all the experimental and numerical works.

Finally, Chapter 6 concludes the thesis with a summary of the key findings in addition to the proposed future work.

Chapter 2. Literature Review

This chapter presents an overview of the boundary layer separation issue, and the proposed techniques that have been suggested in literature, of which many among them have already been implemented in attempt to control boundary layer. The chapter is concluded with a glimpse of the recent works relevant to the area.

2.1. Boundary Layer Control

2.1.1. Flow over an airfoil. The flow over an airfoil - similar to other solid bodies- develops a velocity profile in the boundary layer due to viscosity effects. The layer of air farthest from the airfoil wall has a velocity identical to the freestream velocity U_∞. The closer the air layer to the airfoil wall is, the lower the velocity becomes, until it eventually gets to a velocity of zero where it touches the wall due to viscosity effects, which is also known as the no-slip condition [3]. Therefore, the boundary layer is the region of flow where viscosity effects are significant due to wall shear stress. The resulting drag from this resistance is called the skin-friction drag [4].

2.1.2. Flow separation. When a fluid flows over an airfoil, its particles get slowed down by wall friction. Beyond the point of minimum pressure, the flow particles momentum is decelerated due to wall shear as well as pressure gradients [5]. This is the critical point where flow separates from the airfoil's upper surface. The separated region between the airfoil and the flow stream is an adverse pressure region. As this region gets enlarged, it results in a surge in the resulting pressure drag [6].

At an increased angle of attack (greater than 15° for most airfoils as shown in Figure 2.1), a complete separation of flow may occur. This results in drastic reduction of lift. In such case, the airfoil is said to be stalled [7].
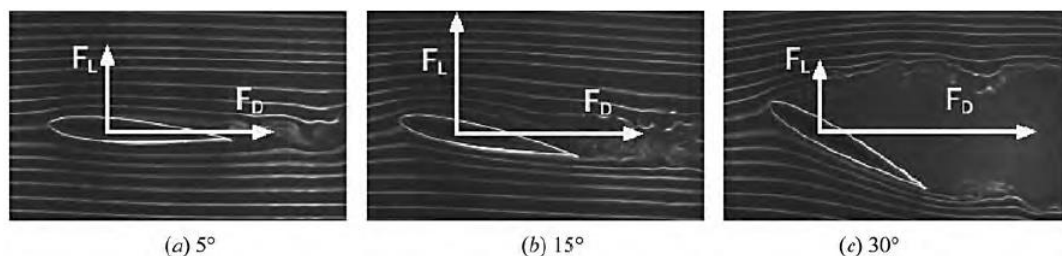
Figure 2.1: Complete flow separation at angles of attack higher than 15°[8].

2.1.3. Methods of controlling boundary layer. Due to this problem, multiple techniques have been developed in order to manipulate and control the boundary layer. The main purpose is to increase the lift and/or decrease the drag. The two boundary-layer phenomena for which the boundary-layer control is desired are transition of laminar flow to turbulent flow, as well as flow separation from the surface. By maintaining the flow in a laminar state, the skin friction can be reduced. And by preventing separation, the lift can be increased. Few notable methods used for boundary layer control are briefly described in the coming subsections.

2.1.3.1 *Controlling transition by shaping the airfoil.* Streamlining the geometry is one way of reducing the pressure drag component attributed to separation and is a quite old method dating back to prehistoric times. Yet using different airfoil geometries helps manipulate the pressure gradient produced by the flow on the airfoil's upper surface. The airfoil can be shaped such that the point of minimum pressure is pushed to the aft of the leading edge. Beyond this point, the adverse pressure gradients become steeper [9]. This is illustrated Figure 2.2; airfoil 1 in Figure 2.2(a) has a

(a) Airfoil 1:
maximum thickness around 0.25c   **(b) Airfoil 2:**
maximum thickness around 0.50c
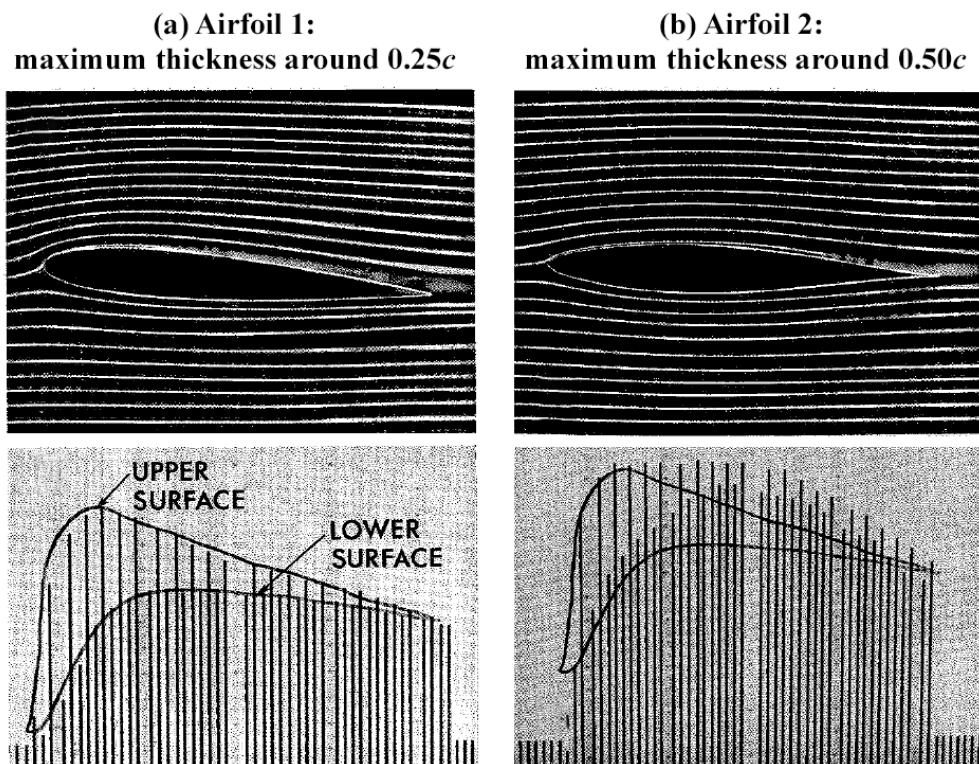
Figure 2.2: Flow visualization and pressure distribution of two airfoils with maximum thickness at different chord lengths (a) Laminar flow extends to nearly 25% of the chord length (b) Laminar flow extends to nearly 50% of the chord length [9].

18

maximum thickness around 25% of the chord length or $0.25c$. Its minimum pressure point is near the leading edge. While the airfoil in Figure 2.2(b), which has a similar lift as the latter, has a maximum thickness at about 50% of the chord length, or $0.5c$, and its lowest pressure point is farther.

Shaping the airfoil is not always advantageous. While this can be helpful at some angles of attack, it could worsen the situation at other angles. At a larger angle of attack, the point of translation to turbulence of the same airfoil in Figure 2.2(b) would move toward the leading edge, leaving the whole upper surface covered with turbulent flow.

2.1.3.2 *Controlling transition and separation by suction.* Suction reduces the thickness of the boundary layer by removing the low-momentum fluid next to the surface. This improves flow stabilization since a thin boundary layer is less likely to become turbulent. It therefore delays the transition to turbulence. Suction is applied through porous surfaces or a series of finite slots [10].

If an airfoil equipped with suction is adjusted at a high angle of attack, suction can help keep the flow attached to the airfoil even beyond the angle where stall occurs without suction (Figure 2.3) [9].

2.1.3.3 *Controlling separation by variable geometry.* Introducing a change in the airfoil geometry helps avoid laminar separation like those that occur at the sharp leading edge of a thin profile. The deflection of a nose flap (Figure 2.4) helps alter the pressure field [9]. Vortex generators can help delay separation by mixing high-

[a] No suction

[b] Suction applied

suction devices
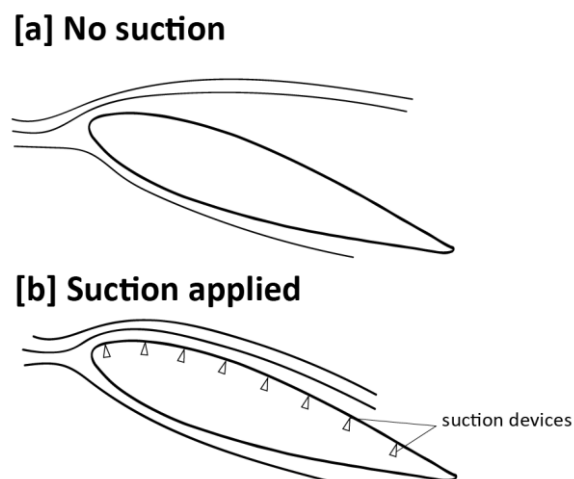
Figure 2.3: Airfoil at a high angle of attack. (a) No suction. Flow is entirely separated (b) Suction applied. Flow is attached to the airfoil.

[a]

[b]
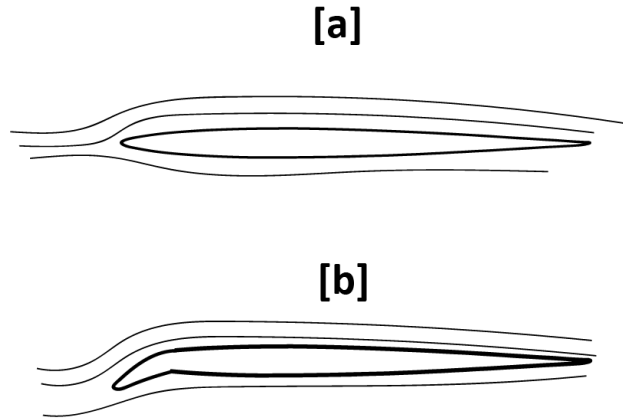
Figure 2.4: Thin airfoil with (a) No deflection, separation occurs at leading edge (b) With deflection, flow remains attached.

momentum fluid from the outer flow with low-momentum flow adjacent to the airfoil surface [5].

      2.1.3.4 *Controlling separation by blowing.* Blowing jets directed into critical areas are useful as well. These can be created by utilizing the pressure differences that exist on the aerodynamic bodies themselves. A good example is a leading-edge slot (Figure 2.5). When the slot is open, it leads air from the region close to the stagnation point through a converging channel and ejects it at high speed at a point of low pressure on upper surface [11][12].

      2.1.3.5 *Moving surface boundary layer control.* Boundary layer exists because of a difference in velocity between flow and the solid wall. Therefore, if the velocity difference is to be removed, the boundary layer can be eliminated. This can be achieved by moving the wall with the direction of the flow.
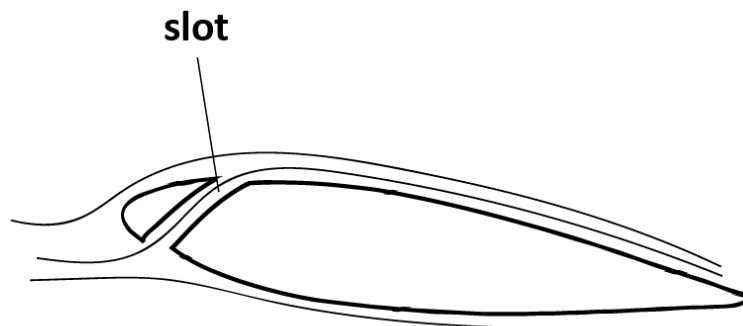
slot

Figure 2.5: A leading edge slot aids in keeping the flow attached by directing it from the stagnation point towards a point of low pressure on the upper surface.

Examples include adding rotating cylinder(s). Cylinders can be added at leading or trailing edge, or a combination of both, but they were found to be more effective in delaying flow separation - and eventually, delaying stall- when placed at the leading edge [13]. Adding a belt moving on two rollers on the upper side of the airfoil is one other example that was investigated by A. Favre [14].

This research focuses on the boundary layer control method mentioned in the latter section; moving surface boundary-layer control, particularly a rotating cylinder placed at the leading edge. The rotation of the cylinder contributes in eliminating velocity difference between the airfoil wall and the flow, resulting in enhancement of aerodynamic performance. This method has also been compared with the suction one. It was found that the rotating cylinder method is three times more efficient in terms of required power [15].

2.2. Related Work

The earliest known commercial application that made use of rotating cylinders is the Buckau rotor ship invented and built by Anton Flettner in 1924. This ship excerpted its propulsion force from the airflow around two large rotating cylinders. The Buckau ship served as an inspiration for scientists and engineers to investigate using rotating cylinders in aerodynamic applications [15].

Following that, experiments by Wolff and Koning [16][17] investigated the effect of adding a rotating cylinder to the leading-edge of an airfoil at different wind speeds. The cylinder rotation accomplished a notable increase in the lift at different wind velocities.

Tennant et al. [18] implemented a rotating cylinder at a symmetrical airfoil's truncated edge. They found that the lift coefficient increased linearly with increasing velocity ratio ζ. They also did a numerical simulation of the rotating cylinder, the airfoil, and the gap between them, using the method of Cebeci-Smith model, the results showed a good correlation with experimental data [19].

Mokhtarian [13] conducted the most descriptive experimental study, complimented by flow visualization and numerical models of Joukowsky and NACA airfoils with rotating cylinders placed at different locations; leading edge, trailing edge, and the upper surface of the airfoil. He also investigated a scooped cylinder and

compared its performance with the normal cylinder shape. The maximum lift obtained was $C_L = 2.22$, which was about 2.6 times that of the base airfoil. The maximum stall was delayed to around 45°. It was shown that the performance improved with higher cylinder-to-freestream velocity ratio ζ up until a certain ratio ($\zeta > 5$), where the benefit of the cylinder rotation diminished and became negligible. The location of the cylinder also played a role in increasing the lift as when the cylinder was placed on the upper side of the leading edge.

The performance of the leading-edge cylinder was also dependent on the cylinder's geometry. A scooped cylinder improved performance at ratios of ζ less than or equal to 1. However, at higher ratios, the geometry of the cylinder was insignificant and showed no particular advantage. The rotating cylinder at the trailing-edge acted like a flap by shifting the C_L vs. α plots to the left, thus increasing the lift coefficients at angles of attack before stall. Therefore, if combined with the leading-edge cylinder, it can significantly improve the performance at small to moderately high angles of attack ($\alpha \leq 18°$).

Mokhtarian's numerical model predicted a maximum lift coefficient with a reasonable accuracy, however, it could not estimate the stall due to the unsteady flow's separation and reattachment, resulting in a bubble, which the numerical method could not quite model accurately back then.

Al-Garni et al. [20] also performed an experimental work of studying the flow over a NACA0024 airfoil equipped with a rotating cylinder at the leading edge, and a flap at the trailing edge. Results showed that a flap angle of $\delta = 0°$ (i.e. base airfoil) the maximum lift coefficient increased from 0.85 to 1.6 as the velocity ratio ζ increased to 4, which is about a 92% increase. The stall angle of attack also showed a 160% increase, and got delayed to around 30-35° at $\zeta = 4$. The downside is that the drag coefficient was increased with increasing ζ. Yet the lift-to-drag ratio was increased to around 20 at a zero angle of attack. Increasing the flap deflect angle to δ=30° helped increase the lift coefficient further to 1.93 when the cylinder is rotated at $\zeta = 4$ compared to 1.24 at $\zeta = 0$, which is about a 56% increase. But the total increase is about 130% due to the combined effects of the high ζ and increase of flap deflect angle. The increased flap angle induced a 10% decrease in the lift to drag ratio, however.

An alike study was done by Modi et al. [21]. The stall angle was delayed from $\alpha = 10°$ to $60°$, with a more than 200% increase in the lift coefficient at a high angle of attack (around $30°$). A reduction in drag coefficient was also observed with the usage of a splined cylinder. In addition, they studied the effect of the cylinder's surface roughness on lift and drag coefficients and showed that the cylinder with the highest surface roughness experienced the highest air torque.

Several numerical studies have been conducted as well; their results were compared with experimental data for validation purposes. Sahu and Patnaik [22] did a numerical simulation of a NACA0012 airfoil with a rotating leading-edge cylinder. They validated their simulation with experimental results carried by Greenblatt and Wygnanski. [23]. The simulation was done at a Reynolds number of $Re = 2.4 \times 10^5$, SST $k - \omega$ model yielded better predictions than other models. The value of lift coefficient improved with increased ζ values, accompanied by a decrease in drag force, which resulted in a high-performance airfoil with delayed stall.

Zhuang et al. [24] also did a numerical study on leading-edge rotation for both two-dimensional NACA63418 airfoil section. Flow separation for the airfoil section was observed to occur at smaller angles of attack on the pressure side of the airfoil near the clearance between rotating cylinder and stationary airfoil. The aerodynamic performance of the leading-edge rotation wind turbine showed enhancement in efficiency at high tip speed ratios. They also studied an application case of a three-dimensional two-bladed wind turbine rotor. They concluded that the power output of the turbine can be optimized through adjusting the cylinder's rotational speed in various wind speeds.

Sankar et al. [25] conducted computational work using combined Blade-Element Momentum on an application of a horizontal wind turbine of 2 blades with rotating leading-edge cylinder as well. The lift and drag characteristics were generated using numerical data from the studies of Zhuang et al. [24]. Their findings using numerical approach were that the airfoil without a rotating cylinder would stall at an angle of $\alpha = 8°$, and the maximum lift coefficient would be about 0.65. However, when the leading-edge cylinder is rotated, the maximum lift coefficient would be around 1.28 and the airfoil would not stall until about $\alpha = 16°$. They also reported that power production suffers due to the low lift to drag coefficient when the cylinder is not in

motion. Yet with the rotation of the cylinder, the peak power produced was 17 kW compared to 2.5 kW without rotation. The stalling of the rotor is delayed to higher wind speeds as well.

Nazari [26] did a numerical study as well on a NACA0024 airfoil with a leading edge rotating cylinder using ANSYS CFX software and validated them with experimental data by Al- Garni [20]. Two turbulence models were used to simulate the flow over the airfoil section, the Shear Stress Transport (SST) model and the Detached Eddy Simulation (DES) model. The latter was used to analyze the flow field in the wake region and vortices created due to flow separation. The lift coefficient increased by 60% and the stall angle by approximately 80% with the rotation of the cylinder in comparison with the original airfoil. A second rotating cylinder near the leading edge was added to the same model with an additional flap. This new model was analyzed using the SST model. The stall angle increased by 90% in comparison with the original airfoil in this case.

Through reviewing the works already done on the matter, it is apparent that the focus has mainly been on proving that the rotation of the cylinder does increase the lift and lift-to-drag ratio. Indeed, that has been proven with multiple experimental works mentioned earlier. Numerical simulations have also worked on replicating the experimental conditions while going to limits that could not be reached in reality due to experimental limitations. The focus in numerical works is, again, primarily about the relation between cylinder rotation and its effect on lift coefficient. Yet little research has been done about the effect of the cylinder's exposure on its aerodynamic behavior. This research will be numerically tackling this case using CFD after validating the numerical model with experimental data, including proving the improved aerodynamic performance with increased cylinder rotational speed.

Chapter 3. Experimental Setup and Theoretical Formulation

3.1.   Overview

Experiments were conducted in a suction-type, subsonic, open-loop wind tunnel. The test section has a cross-sectional area of 0.9×0.7 m, and a length of 1.8 m (Figure 3.1).

(a)

(b)

Figure 3.1: (a) Wind tunnel in which the experiments on the airfoil were conducted (b) Testing section dimensions.

A NACA0024 airfoil wing model has been used for the experiments (Figure 3.2). The airfoil is symmetric and has a chord length of 20 cm and a maximum thickness of 4.8 cm at 30% of the chord length. A total of 22 pressure taps were distributed equally on the upper and lower surfaces of the airfoil, with 11 taps on each surface. The pressure taps cover a length of 6 cm (of chord length) from the region at the middle of the span, extending from 25% to 55% of the chord length, with a 0.6 cm distance between each two holes. The model is made of wood that has been smoothed to minimize the friction with air at the surfaces.
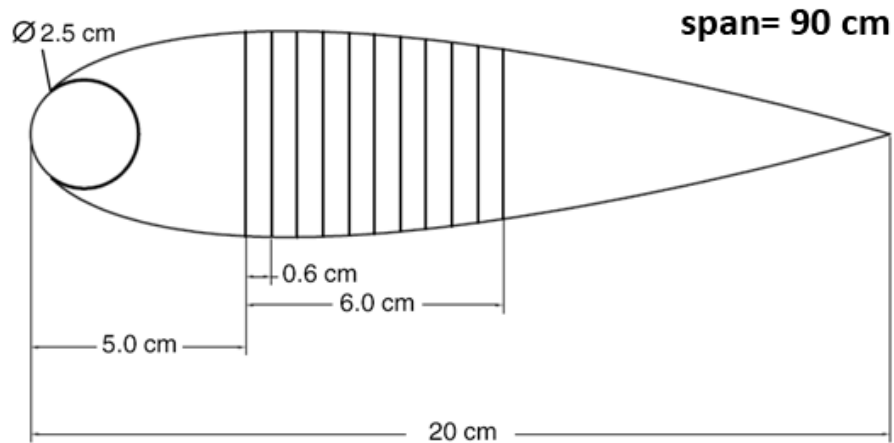
Figure 3.2: Cross-sectional view of the experimental NACA0024 model with pressure taps indicated.
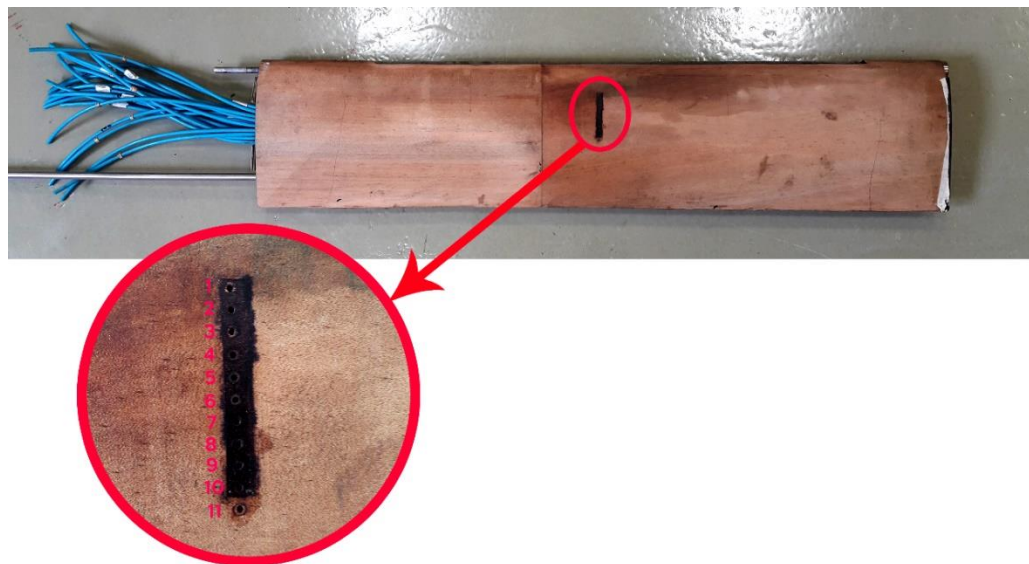
Figure 3.3: The top view of the wing model with a zoom on the numbered pressure taps.

A 25 mm solid steel cylinder has been affixed at the airfoil's leading edge, as shown in Figure 3.4. The cylinder is coupled with a variable speed electric motor that provides the drive for rotation (Figure 3.5). The geometry of the NACA0024 airfoil model used for the experiments initially had a cylinder exposure of 15% as shown in Figure 3.2. However, it was later modified to be 25.5%. The modified cylinder exposure of the wing model is shown in Figure 3.4, and the updated cross-sectional view is shown in Figure 4.4. Although the wood on the upper side of the cylinder exposure was smoothed, it still was not perfectly streamlined, and a step of around 1 mm existed on the model.
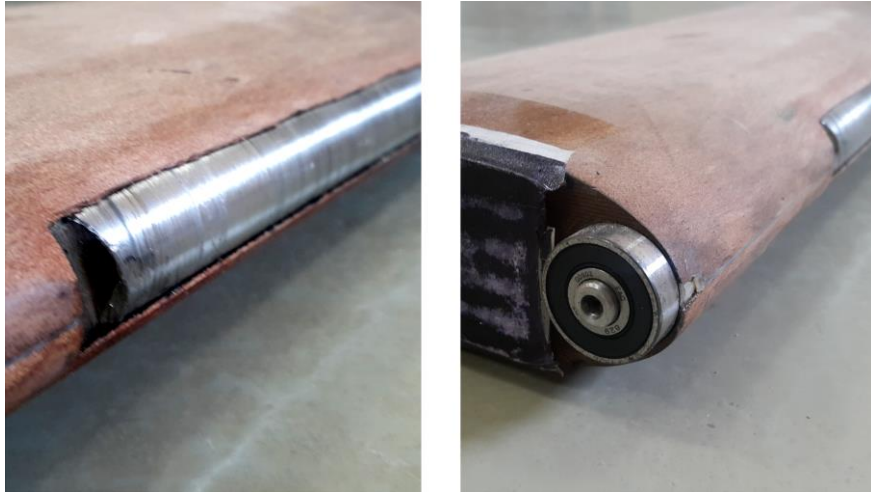
Figure 3.4: Cylinder mounted at the airfoil's leading edge, with a 25.5% exposure.

Figure 3.5: Motor used for driving the rotation of the cylinder.

The tests have been performed at a freestream flow velocity of 5 m/s, and the angle of attack was varied between 0° and 15° with 5° increments. The cylinder was driven to rotate at speeds alternating from 0 to 7250 rpm, which consequently correspond to ζ values of about 0 to 2. The lift and drag forces –and their corresponding coefficients – were calculated through integration of the measured static pressures over the model's upper and lower surfaces.

3.2. Pressure Measurement

A DSA 3200 Scanivalve was used to measure the pressures on the airfoil's upper and lower surfaces. The data was collected and analyzed through DSA LabVIEW 2009 Utility PC software (Figure 3.6). Pressure values were recorded at a time interval of 1500 ms, with 30 frames for each measurement.

For measurement of freestream pressure, a pitot tube (Figure 3.7 (a)) and pressure transducer were used. The pressure transducer gives readings of static pressure, volumetric flow rate, and flow velocity. Therefore, it served in measuring the freestream velocity. Figure 3.7 (b) shows the pressure taps connected to the Scanivalve.

Figure 3.6: DSA LabVIEW software used for collecting pressure data.

3.3. Flow Visualization Method

Flow visualization is an essential step to apprehend the eddy motion and turbulence of flow around the airfoil. The interpretation of the still images obtained through flow visualization allows understanding of the physics of the flow field. Multiple techniques are used to visualize the flow, examples include but are not limited to: hydrogen bubble visualization, dye and smoke visualization, and digital particle velocimetry [27].

The smoke wire method was used to visualize flow around the airfoil model. A pair of 2.59 mm Nichrome wires were placed ahead of the leading-edge. In addition to that, a honeycomb setup was placed at the inlet of the wind tunnel to assist in streamlining the flow. The wires were coated with a Risella X420 oil that is heated by a voltage source of 17 volts in order to produce the required smoke for visualization. The freestream flow velocity was set to 1.7 m/s during this procedure, as this speed has

(a)
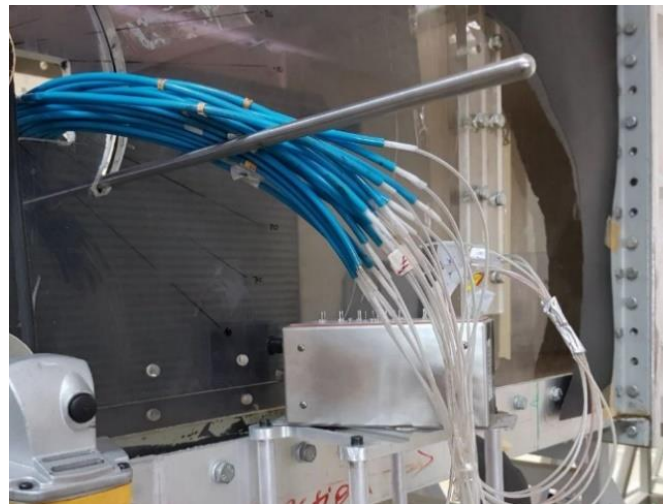
(b)

Figure 3.7: (a) Pitot tube hanging from the upper wall of the wind tunnel, positioned in the direction of the flow (b) Pressure taps of the airfoil connected to DSA 3200 Scanivalve device [43].

been determined to be the most suitable for producing a well-defined view of the streamlines formed by smoke without disrupting them.

3.4.   Experimental Procedure

The tests were done at an air temperature of 26℃, corresponding to a density $\rho = 1.18 \, \text{kg/m}^3$, and dynamic viscosity $\mu = 1.841 \times 10^{-5}$ Pa.s [2]. The wind tunnel was run at 5 m/s, and the angle of attack was varied from 0° to 15° with increments of 5° to. The flow was captured for ζ values of 0, 1 and 2. This ratio was restricted by two parameters: flow velocity and cylinder rotational speed. Going beyond these restrictions causes oscillations and vibrations, which would disturb the pressure

readings. Table 3.1 summarizes the conditions at which the experiments were conducted. For visualizing the flow, a camera was secured at an untouched position and angle, facing the side view of the wind tunnel, and focused mainly on the on the upper airfoil surface in order to have a clearer image of the separation. Still shots were later obtained from the videos to show the behavior of the flow.

Table 3.1: Conditions at which the experimental tests for measurement of pressure have been performed

Freestream velocity, U_∞	5 m/s
Freestream static pressure, $P_{S,\infty}$	14.75 Pa
Freestream Dynamic Pressure, $P_{D,\infty}$	15 Pa
Angle of attack, α	$0° - 15°$ (5° increments)
Cylinder-to-freestream velocity ratio, ζ	0, 1, 2

3.5. Data Analysis

3.5.1. Pressure and skin-friction coefficients. The pressure coefficient was calculated according to the following equation [28]:

$$c_P = \frac{P - P_{S,\infty}}{P_{D,\infty}} \tag{1}$$

Where $P_{D,\infty}$ is the freestream dynamic pressure and is calculated as [28]:

$$P_{D,\infty} = \frac{1}{2}\rho U_\infty^2 \tag{2}$$

The skin friction coefficient is calculated through [29]:

$$c_f = \frac{\tau}{P_{D,\infty}} \tag{3}$$

Where τ is the shear stress acting tangentially on the airfoil along the streamlines of the flow, and is defined as [29]:

$$\tau = \mu \frac{dU}{dy} \tag{4}$$

With μ being the viscosity coefficient, and $\frac{dU}{dy}$ the velocity gradient.

3.5.2. Lift and drag coefficients. Flow over an airfoil generates two types of aerodynamic forces; the shear force, which is tangent to the surface and points to the positive direction, and the pressure force, which acts normal on the surface and points to the negative direction, as shown in Figure 3.8.
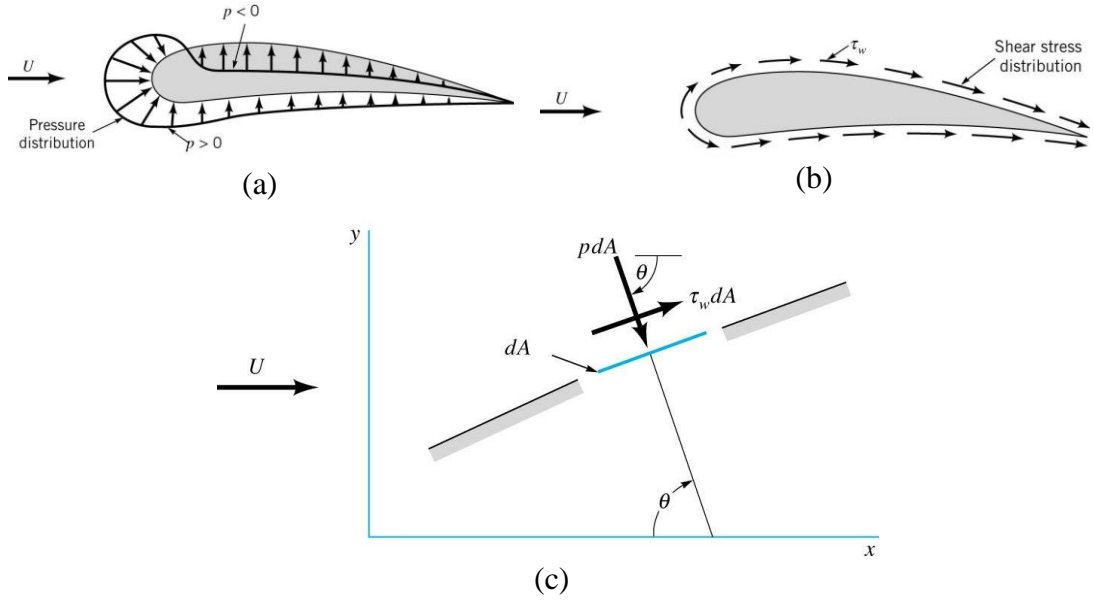
Figure 3.8: A schematic representation of (a) Pressure forces, (b) Shear forces, and (c) Pressure and shear forces direction at a surface with local inclination angle θ [30].

Generally, the overall aerodynamic forces acting on an airfoil can be separated into two components: axial and normal (Figure 3.9). The axial force is parallel to the surface, and the normal force is perpendicular to it. The lift force exerted on the airfoil equals the sum of the vertical components of these two forces, while the drag force equals the sum of their horizontal components. The coefficients of the normal force, C_N, and the axial force, C_A, can be calculated as follows [29]:

$$C_N = \int_0^{x/c} \left(c_{P,l} - c_{P,u}\right) d\left(\frac{x}{c}\right) + \int_0^{x/c} \left(c_{f,u}\frac{dy_u}{dx} + c_{f,l}\frac{dy_l}{dx}\right) d\left(\frac{x}{c}\right) \tag{5}$$

$$C_A = \int_0^{x/c} \left(c_{P,u}\frac{dy_u}{dx} - c_{P,l}\frac{dy_l}{dx}\right) d\left(\frac{x}{c}\right) + \int_0^{x/c} \left(c_{f,u} + c_{f,l}\right) d\left(\frac{x}{c}\right) \tag{6}$$

Where $c_{P,u}$ and $c_{P,l}$ are the pressure coefficients on the upper and lower airfoil surfaces, respectively. $\frac{dy_u}{dx}$ and $\frac{dy_l}{dx}$ are the geometry inclines, or slopes, of the upper and lower surfaces, respectively. And $c_{f,u}$ and $c_{f,l}$ are the skin friction coefficients of the upper
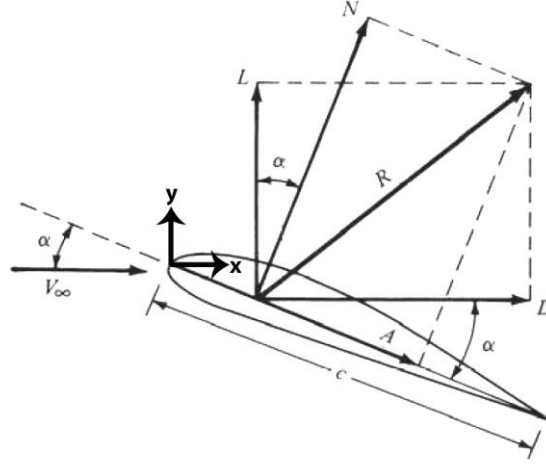
Figure 3.9: A schematic representation of the aerodynamic forces acting on an airfoil when experiencing a fluid flow [27].

and lower surfaces, respectively. The integrations are computed along the full non-dimensional fractions of the chord length, x/c.

The slopes $\frac{dy_u}{dx}$ and $\frac{dy_l}{dx}$ have been calculated through the geometry of the airfoil, defined by the following function for a symmetric airfoil [31]:

$$y = 5t\left[0.2969\sqrt{\frac{x}{c}} - 0.1260\left(\frac{x}{c}\right) - 0.3156\left(\frac{x}{c}\right)^2 + 0.2843\left(\frac{x}{c}\right)^3 - 0.1015\left(\frac{x}{c}\right)^4\right] \quad (7)$$

Where t is the maximum thickness of the airfoil as a fraction of the chord. For the NACA0024 airfoil under study, the maximum thickness is 0.048 m, therefore, this value is 0.24. And the slopes are thus calculated according to the slope formula:

$$m = \frac{y_2 - y_1}{\left(\frac{x}{c}\right)_2 - \left(\frac{x}{c}\right)_1} \quad (8)$$

The integration in equations (5) and (6) is done numerically using the trapezoidal rule:

$$I = \frac{h}{2}\left[f(x_0) + 2\sum_{i=1}^{n-1} f(x_i) + f(x_n)\right] \quad (9)$$

Eventually, the lift and drag coefficients, C_L and C_D can be computed according to:

$$C_L = C_N \cos(\alpha) - C_A \sin(\alpha) \quad (10)$$

$$C_D = C_N \sin(\alpha) + C_A \cos(\alpha) \quad (11)$$

with the sign convention for α being positive for clockwise direction.

32

Chapter 4. Numerical Methodology

In this chapter, a numerical analysis is conducted on a NACA0024 airfoil using ANSYS FLUENT 17.0. A 2D model has been employed, since the flow is of a two-dimensional nature, and the main focus is on boosting the lift force in the 2D domain. It is thus needless to carry a three-dimensional analysis as that requires compelling computing power and more complex meshing techniques, in addition to longer computing times. To reduce the computation time, mesh independence analysis has been deployed to diminish the effect of the mesh size on the results. After mesh independence has been achieved, the numerical simulation has been validated against earlier experimental work. Finally, the numerical simulation is used to conduct a parametric study beyond the experimental limit of $\zeta \leq 2$. Furthermore, the validated numerical model is used to study the effect of changing the percentage of cylinder exposure on the aerodynamic performance. A second-order accurate steady implicit formulation has been employed throughout with the standard under-relaxation parameters. The solving residuals criteria have been set to 1×10^{-6} for all variables.

4.1. Resolving the Boundary Layer

In the case of an external flow, such as that over an airfoil, the flow starts laminar at the leading edge, where it is dominated by viscous forces. However, as it moves over the surface, viscosity forces start diffusing inside the fluid, and this drains the energy of the flow causing the fluid particles to become chaotic, which results in flow transitioning to a turbulent state. The region where the velocity deformation occurs is known as the boundary layer. For a flow over a flat plate, the boundary layer is generally assumed to be laminar up until $Re = 1 \times 10^5$, which is known as the critical Reynolds number [2]. Airfoils can be approximated as flat plates, but the curvature of their surfaces essentially denotes that their critical Reynolds number is less than the that of a flat plate [32].

In numerical simulations, resolving the near-wall regions of a turbulent boundary layer is critical for the solution to produce the correct flow behavior [33]. The flow near the wall can be treated in two different approaches; employing logarithmic-based wall functions, or resolving the viscous sublayer flow, as shown in Figure 4.1. The non-dimensional wall distance value, wall y$^+$, of the first grid cell near the wall is

important when deciding between the two approaches. In logarithmic-based wall functions approach, the first cell must have a y^+ value between 30 and 300. However, for the viscous sublayer approach, the first cell ought to have a y^+ value of 1 or less [34].
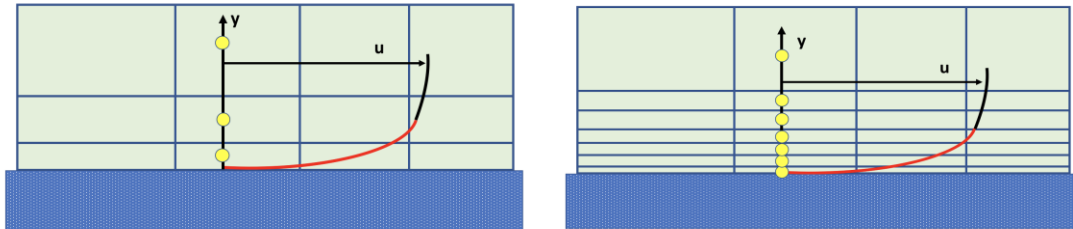

Figure 4.1: Resolving boundary layer near-wall mesh using (a) logarithmic-based wall functions or (b) viscous sublayer approach [35].

In CFD simulation, selecting the most appropriate wall treatment approach depends on the nature of the simulated problem. When separation does not affect the flow behavior (Figure 4.2a), employing logarithmic-based wall functions would be applicable and would aid in reducing mesh size and computation time without compromising the boundary layer profile results. However, when flow separation is existent and is influencing the flow behavior, implementing logarithmic-based wall functions does not provide a correct prediction of the boundary layer profile. Instead, resolving the viscous sublayer cells directly tends to offer a more accurate solution [34].
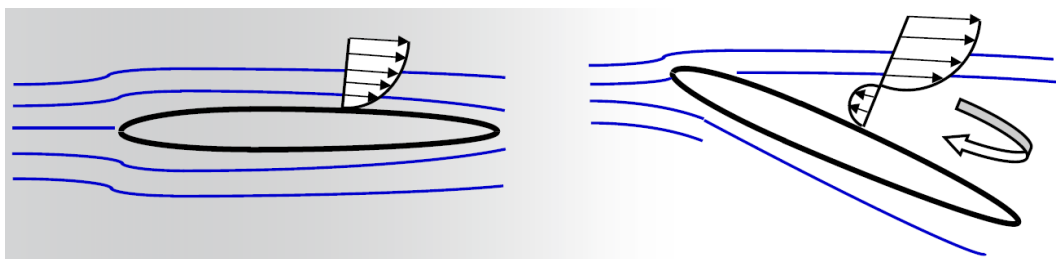
Figure 4.2: Schematic diagram for flow over airfoil. (a) Flow with separation where logarithmic-based wall functions is applicable (b) Flow with separation where logarithmic-based wall functions is not applicable [34].

4.2.   CFD Model

A base CFD model was first created for the purpose of validation of numerical results through comparing them with their experimental counterparts. The conditions of this model were set in a way that replicates the actual conditions of the test conducted in the lab.

4.2.1. Meshing and geometry. The mesh was constructed with triangular elements for the domain surrounding the airfoil, as shown in Figure 4.3. The height of the domain was set to 700 mm similar to that of the lab's wind tunnel, and the radius of the inlet side was set to 350 mm.

The mesh consists of two regions; the first being the circular domain surrounding the airfoil, and the second is the rest of the domain. The circular domain was added in order to enable rotational mesh motion such that the airfoil's angle of attack can be changed during simulation.
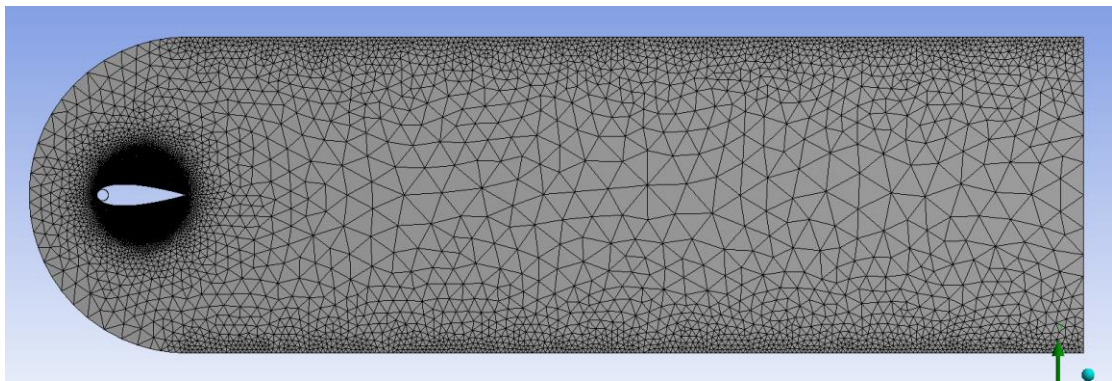
Figure 4.3: The two mesh domains.
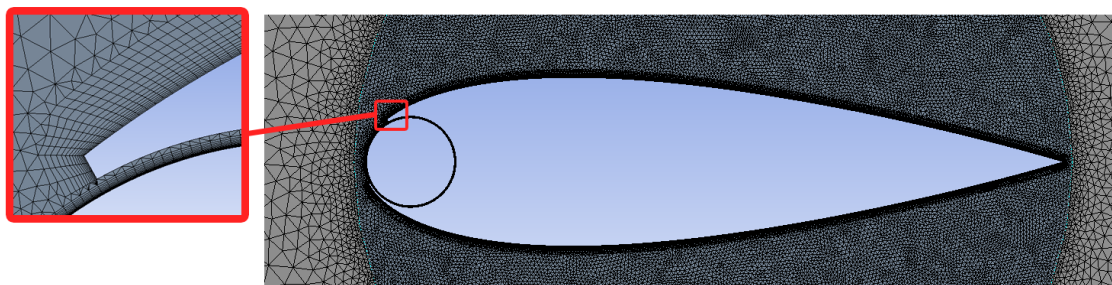
Figure 4.4: Airfoil geometry and mesh of 25.5% nonsymmetric cylinder exposure, with sharp step at the airfoil's upper surface.

The geometry of the airfoil has been made to match that of the model used in the experiments which has an exposure of 25.5%, and a sharp step at its upper exposure edge (Figure 4.4). The model's exposure is non-symmetrical; when going from the center of the circle, the exposure is 7.8% towards in the lower half of the cylinder and 17.8% in the upper half.

An inflation layer with 2 mm width was added around the airfoil walls to achieve extra resolution in order to capture the behavior at the boundary layer, as it is the part of utmost importance in the flow (Figure 4.4). In order for the first grid cell of

the boundary layer in the near-wall region to have a y^+~1, the thickness of this specific cell was calculated to be 0.025 mm. The density and viscosity of air were changed to match the experimental conditions mentioned in chapter 3.

4.2.2. Boundary conditions. The boundary conditions were also set to replicate the experimental conditions: An inlet velocity of 5 m/s in the x-component, which corresponds to a low Reynolds number of $Re = 6.4 \times 10^4$. The cylinder was set to moving-wall with no-slip condition, and with absolute clockwise rotation in rad/s corresponding to the experimental values shown in Table 4.1, the negative sign indicates a clockwise rotation. The outlet boundary condition was left at a 0 kPa gage pressure.

Table 4.1: Experimental cylinder-to-freestream velocity ratios and their corresponding rotational speeds, negative sign for clockwise direction.

ζ	U_c (rad/s)
0.9294 (≈ 1)	-371.76
1.8904 (≈ 2)	-759.2

To change the angle of attack of the airfoil during flow visualization, the mesh surface surrounding the airfoil was set to rotate -0.0875 rad/s (clockwise direction) - which corresponds to 5°/second - such that the angle of the airfoil increases by 5° every time step. Calculation-wise, however, changing the velocity components at the inlet, based on the corresponding angle of attack, has been found to be more convenient, and simplified the calculation process of lift and drag coefficients.

4.3. Mesh Independence Analysis

To ensure that the generated mesh produces accurate results regardless of the number of elements it includes, a mesh independency analysis has been conducted. Four meshes have been generated and tested the first mesh is a very coarse mesh with 11×10^3 elements, the second is a refined mesh with 40×10^3 elements, the third is a fine mesh of 94×10^3 elements, and the final mesh is an extremely fine mesh with 150×10^3 elements.

The simulation has been executed at an angle of attack of $\alpha = 5°$, and a cylinder-to-freestream velocity ratio of $\zeta = 1$. Boundary conditions remained unchanged to the ones mentioned in the previous section. For the purpose of its

36

robustness and reasonable accuracy, the standard $k - \varepsilon$ model was used for the simulations. The results have been plotted in Figure 4.5. All four cases have demonstrated a similar behavior. Yet it can be seen that after the 94×10^3 elements case, the results do not change much despite refining the mesh and increasing its resolution. Thus, the 94×10^3 elements mesh will be used in this research for carrying out the simulations.
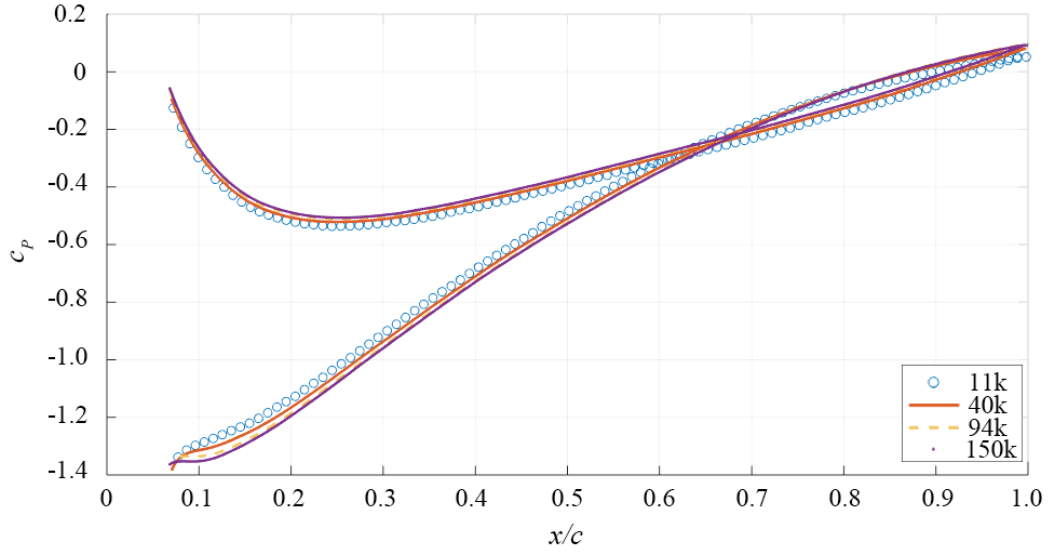

Figure 4.5: Mesh independency plot of c_P versus x/c for different number of mesh elements.

4.4. Turbulence Model Selection

A comparison between different turbulence models has been carried out for the purpose of selecting the most appropriate turbulence model for the case [36]. The simulation was run using four different turbulence models; the two-equations standard $k - \varepsilon$ model and SST $k - \omega$ model, the four-equations Transition SST model, and the five-equations Reynold Stress model. The graph in Figure 4.6 illustrates the outcome of using the four earlier mentioned turbulence models at $\alpha = 5°$ and ζ=1. At the first glance, it can be perceived that the difference between them is negligible, as all of their predictions fall very close to the experimental ones. But it can be said that this comparison does not provide the full picture, since, at this low angle of attack, the flow is fully attached to the airfoil. Hence, it is essential to compare the models at a higher angle of attack, where flow separation is existent. The simulation was, thus, run again for the same turbulence models, but at an angle of attack of $\alpha = 15°$. The results are

37

shown in Figure 4.7. Truly, the differences are much apparent at this case, with the Transition SST model and standard k-ε being the least compliant with the experimental data, and the SST $k - \omega$ providing the closest values to the experimental ones. Indeed, when it comes to selecting the appropriate turbulence model, the Shear Stress Transport (SST) $k - \omega$ is the suggested model to be used for flow separation cases where the viscous sublayer ought to be resolved [37]. Previous studies [22][24][38] reported as well that the SST $k - \omega$ model is quite suitable for simulating this particular case due to its high precision and robustness.

The SST $k - \omega$ is a hybrid turbulence model that combines the $k - \varepsilon$ and $k - \omega$ models. It activates the k-ε model in the regions away from wall, and switches to $k - \omega$ model in the near-wall region through a blending function [39]. The SST $k - \omega$ turbulence model is governed by equations (13) and (14) [40][41].

Turbulence kinetic energy:

$$\frac{\partial k}{\partial t} + U_j \frac{\partial k}{\partial x_j} = P_k - \beta^* k\omega + \frac{\partial}{\partial x_j}\left[(\nu + \sigma_k \nu_T)\frac{\partial k}{\partial x_j}\right] \tag{12}$$

Specific dissipation rate:

$$\frac{\partial \omega}{\partial t} + U_j \frac{\partial \omega}{\partial x_j} = \alpha S^2 - \beta \omega^2 + \frac{\partial}{\partial x_j}\left[(\nu + \sigma_\omega \nu_T)\frac{\partial \omega}{\partial x_j}\right] + 2(1 - F_1)\sigma_{\omega 2}\frac{1}{\omega}\frac{\partial k}{\partial x_i}\frac{\partial \omega}{\partial x_i} \tag{13}$$
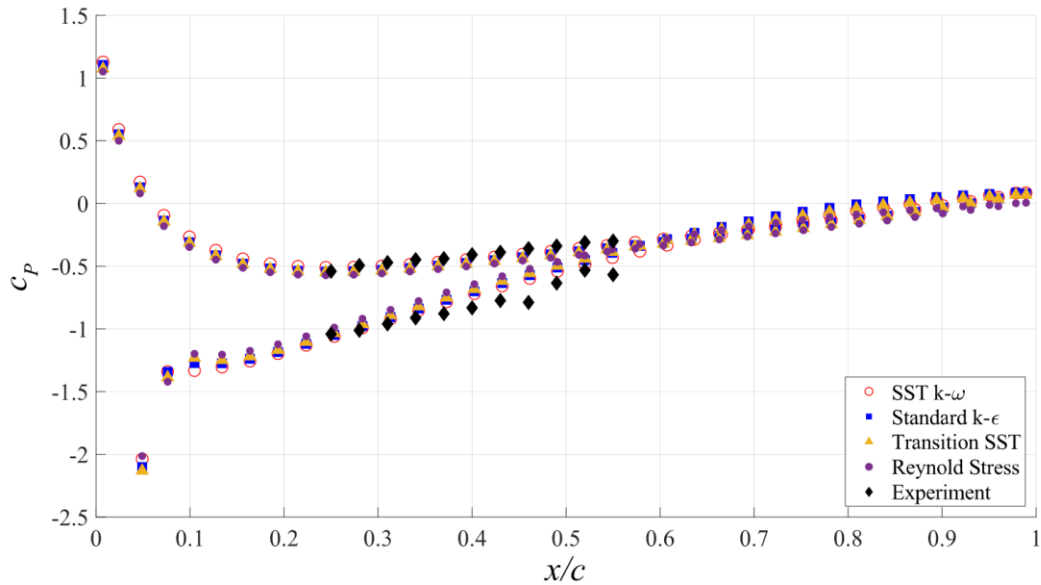

Figure 4.6: c_P versus x/c calculated using different turbulence models with validated with experimental data at $\alpha = 5°$, $\zeta = 1$.
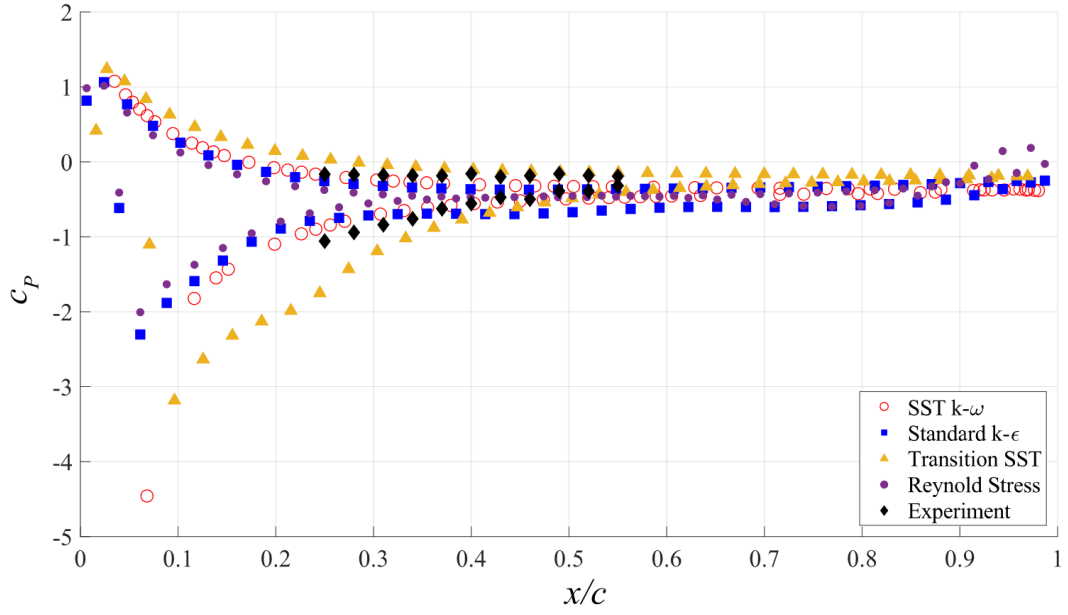
Figure 4.7: c_P versus. x/c calculated using different turbulence models with validated with experimental data at $\alpha = 15°$, $\zeta = 1$.

Where F₁ is the first blending function, which is equal to 1 inside the boundary layer, and equal to 0 outside it:

$$F_1 = \tanh\left\{\left\{\min\left[\max\left(\frac{\sqrt{k}}{\beta^*\omega y}, \frac{500v}{y^2\omega}\right), \frac{4\sigma_{\omega 2}k}{CD_{k\omega}y^2}\right]\right\}^4\right\} \tag{14}$$

And

$$CD_{k\omega} = \max\left(2\rho\sigma_{\omega 2}\frac{1}{\omega}\frac{\partial k}{\partial x_i}\frac{\partial \omega}{\partial x_i}, 10^{-10}\right) \tag{15}$$

v_T is the kinematic viscosity

$$v_T = \frac{a_1 k}{\max(a_1\omega, SF_2)} \tag{16}$$

Where F₂ is the second blending function

$$F_2 = \tanh\left[\left[\max\frac{2\sqrt{k}}{\beta^*\omega y}, \frac{500v}{y^2\omega}\right]^2\right] \tag{17}$$

And P_k is the production limiter

$$P_k = \min\left(\tau_{ij}\frac{\partial U_i}{\partial x_j}, 10\beta^* k\omega\right) \tag{18}$$

With the model constants being $\alpha_1 = \frac{5}{9}$, $\alpha_2 = 0.44$, $\beta_1 = 0.075$, $\beta_2 = 0.0828$, $\beta^* = 0.09$, $\sigma_{k1} = 0.85$, $\sigma_{k2} = 1$, $\sigma_{\omega 1} = 0.5$ and $\sigma_{\omega 2} = 0.856$.

Therefore, the SST $k - \omega$ will be used for simulation validation purposes, in addition to all the rest of numerical studies conducted in this research.

4.5.   Variation of Cylinder-to-freestream Velocity Ratio

The main purpose of building a CFD model is to conduct experiments beyond the limitations imposed by actual testing conditions. One of the main limitations in the experimental part of this research is the vibration and oscillations that take place when the flow velocity or the cylinder-to-freestream ratios are increased. Thus, having validated the CFD model, it is now feasible to conduct further studies beyond those restrictions. One of the most important studies to attempt is increasing the cylinder-to-free-stream velocity ratio, as it is expected to get an enhanced aerodynamic performance with the increase of the cylinder rotational speed.

4.5.1. Geometry and mesh. The geometry of the airfoil was slightly modified in the region where the sharp step was at, the step was replaced by a smooth curve that would allow the flow to pass over it without risking the possibility of separation. Since the flow is quite sensitive to any kind of abrupt change in geometry, it is essential to streamline the surface of the aerodynamic object. The modified geometry is shown in Figure 4.8. As for the mesh, it was left unchanged from the one discussed in earlier sections.
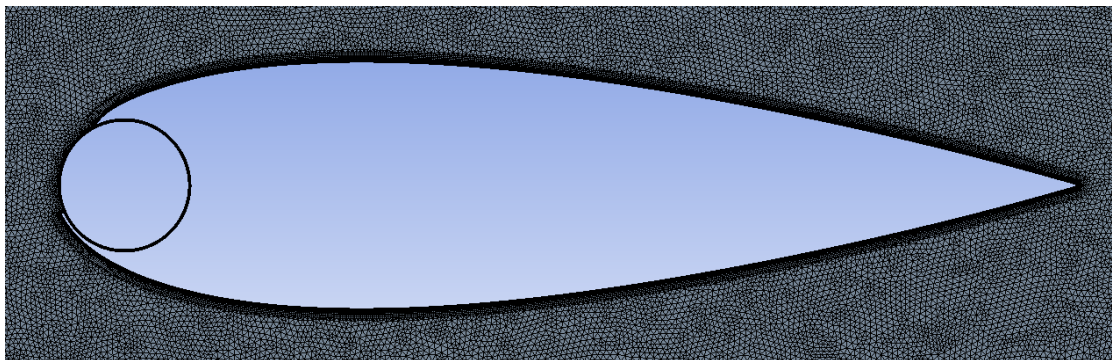

Figure 4.8: Slightly modified geometry where the sharp step was replaced by a smooth curve at the upper side of the cylinder exposure.

4.5.2. Boundary conditions. The inlet boundary condition was set to a velocity of 5 m/s in the x-direction, and the outlet at 0 kPa gage pressure. The cylinder was also

set to a moving wall with no-slip condition, at the rotational speeds shown in Table 4.2. The circular mesh was set to rotate at -0.0875 rad/s to get the airfoil's angle of attack changed by a step of 5° during simulation.

Table 4.2: Numerical simulation cylinder-to-freestream velocity ratios and their corresponding rotational speeds, negative sign for clockwise direction.

ζ	U_c (rad/s)
0	0
1	-400
2	-800
4	-1600
6	-2400

4.6. Alteration of Cylinder Exposure

One additional numerical study to consider is the effect of variation of the cylinder exposure on the aerodynamic performance of the airfoil. In experimental conditions, such study would require manufacturing of multiple models. But the advantage of building a validated CFD model eases such process down to a matter of constructing different geometries. Thus, this section covers three cases of different, symmetric cylinder exposures, and the conditions under which the simulation was implemented.

4.6.1 Geometry. Three different geometries of the 25 mm rotating cylinder have been tested, with each having a symmetric exposure. In the first case, the cylinder has a 20% exposure, and is shown in Figure 4.9 (a). The second case has an exposure of 30%, and is shown in Figure 4.9 (b). Finally, the third and last case has an exposure of 40%, and is shown in Figure 4.9 (c).

4.6.2. Mesh and boundary conditions. In this study as well, the unchanged previously generated mesh was used. The boundary conditions were set to a velocity inlet of 5 m/s in the x-direction, and a pressure outlet of 0 kPa gage. The simulation was run at an angle of attack of $\alpha = 10°$, and the cylinder was set to rotate at -1,600 rad/s, corresponding to a cylinder-to-freestream velocity ratio of $\zeta = 4$.
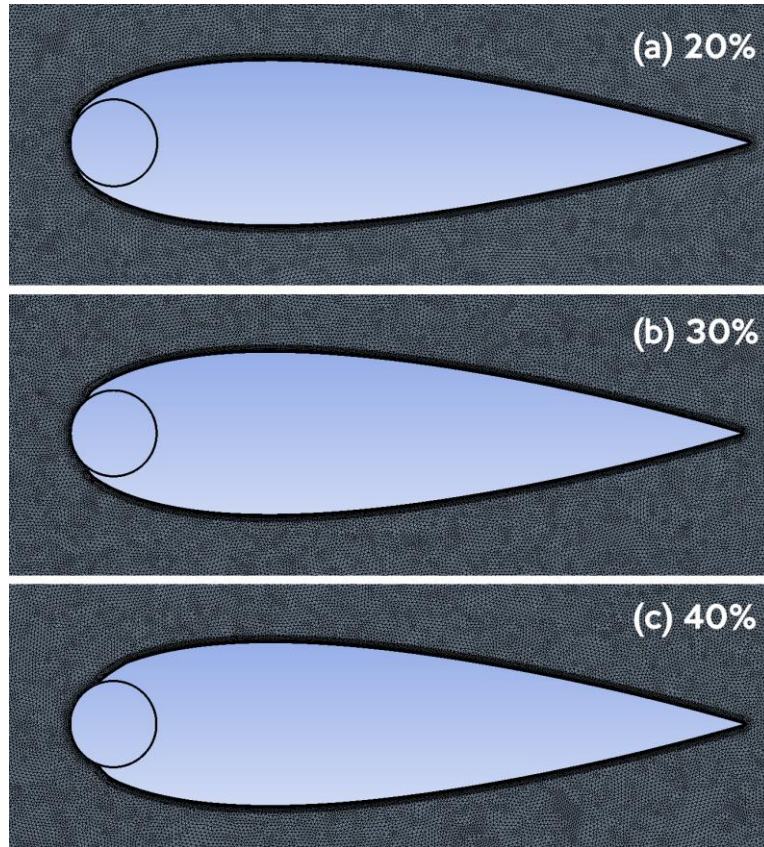
Figure 4.9: Geometries of airfoil leading-edge cylinder with cylinder exposure of (a) 20%, (b) 30%, and (c) 40%.

Chapter 5. Results and Discussion

5.1. Experimental Results

As this work is a combination of experimental and numerical simulation, most of the experimental results will be presented and discussed in the following section, which covers the numerical simulation validation. For this part, it is good to present a summary of the testing results in terms of aerodynamic parameters.

The lift coefficient, drag coefficient, and lift-to-drag ratio have been calculated using equations in section 3.5.2. Figure 5.1 shows the variation of lift coefficient (C_L) as the angle of attack is changed for the three different cases of $\zeta = 0$, 1 and 2. In all three cases, the maximum lift coefficient was attained at $\alpha = 10°$, and started to decrease at $\alpha = 15°$ due to the start of flow separation. It can be seen that, as expected, the rotation of the cylinder enhanced the lift coefficient at all tested angles of attack. Since the NACA0024 is a symmetric airfoil, it exhibits zero lift at $\alpha = 0°$ due to the equivalent pressure distribution on its upper and lower surfaces, but the rotation of the cylinder has enabled a slight increase in the lift coefficient even at such case.
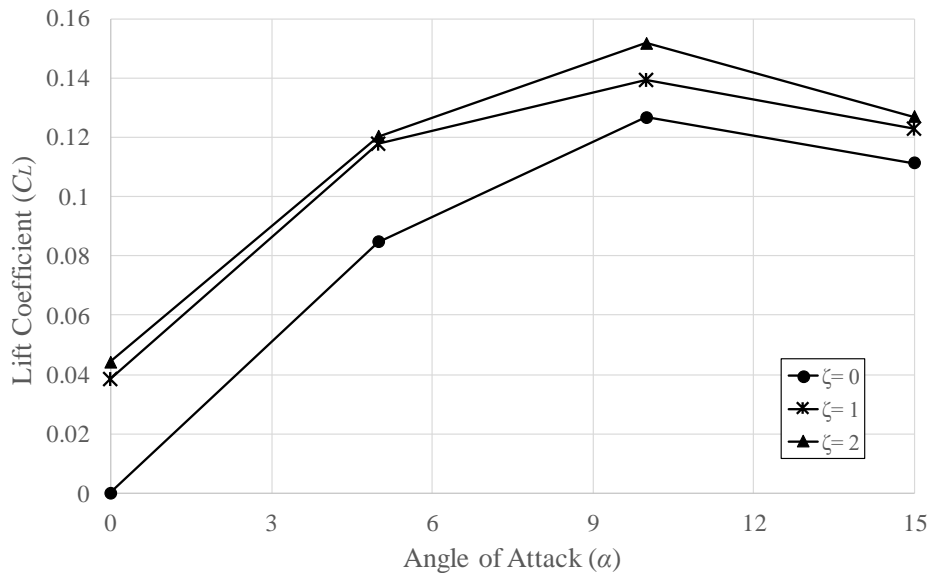

Figure 5.1: Lift coefficient (experimental) versus angle of attack at $\zeta = 0$, 1 and 2.

Similarly, the drag coefficient vs. angle of attack is plotted in Figure 5.2. The drag coefficient (C_D) increases with increasing angle of attack, and the rotation of cylinder induces an increase in the drag as well. This is because the rotation of the
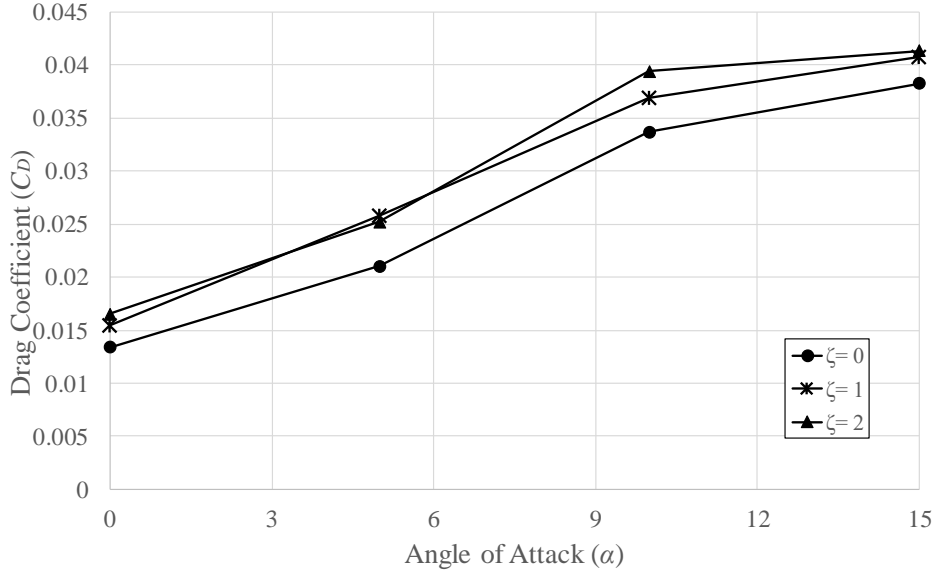
Figure 5.2: Drag coefficient (experimental) versus angle of attack at $\zeta = 0$, 1 and 2.

cylinder serves in decreasing the pressure on the upper airfoil surface while increasing that on the lower surface. Such change in pressure alters the normal component of the force acting on the airfoil, and it can be noted from equation (12) that the drag is directly proportional to $\sin(\alpha)$. Additionally, in Figure 5.3, the lift-to-drag ratio (C_L/C_D) is plotted versus angle of attack. The lift-to-drag ratio is generally a measure of the aerodynamic efficiency of an airfoil, thus, an increase in C_L/C_D denotes an enhanced aerodynamic performance. The experimental results show that this ratio increased, even if slightly, with increased ζ, with the largest value occurring at $\alpha = 5°$.

These experimental results show a good summary of the overall performance of the airfoil; however, they only show a segment of the full picture. The section for which the data were measured and integrated covers only a portion of the airfoil, mainly 25% to 55% of the chord, which is a small section, and is sensitive to the slightest changes in the boundary layer, primarily in terms of flow separation. This is also the reason behind the values of the coefficients being particularly low.

5.2. Numerical Simulation Validation

5.2.1. Pressure coefficient. A comparison of the numerical data with the experimental ones has been made [42]. It is essential to compare the solution obtained from a numerical simulation to judge on its validity and physical meaning. The main variable that was used in validation is the pressure coefficient c_P. It has been plotted
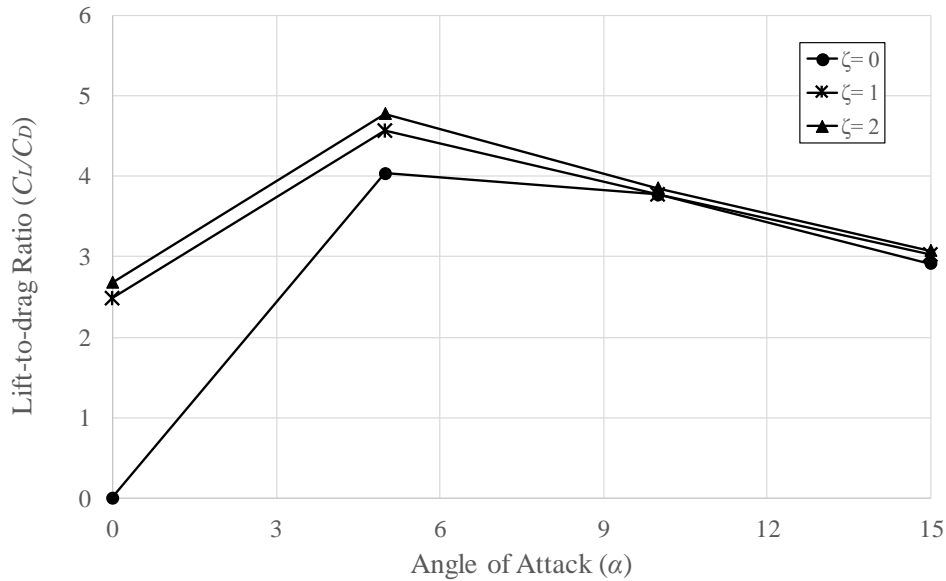
Figure 5.3: Lift-to-drag ratio (experimental) versus angle of attack at $\zeta = 0$, 1 and 2.

over the full range of the chord, i.e. from $x/c = 0$ to $x/c = 1$ for both experimental and numerical cases. Figure 5.4 shows the data plotted for $\zeta = 0$. At $\alpha = 0°$, the pressure coefficient curve for the upper and lower surfaces lie on top of each other, denoting zero lift force, which is as anticipated from a symmetric airfoil. The pressure difference between the two surfaces then starts to be apparent at higher angles of attack. Similarly, Figure 5.5 and Figure 5.6 show the pressure coefficient plots of experimental versus numerical data at $\zeta = 1$ and 2, respectively. All cases show a good correlation between the two. The numerical simulation managed to succeed at exhibiting a similar behavior to the actual values of pressure coefficient. Having validated the results, it can be safely assumed that the simulation has gone in the right direction.

5.2.2. Flow visualization. The experimental and numerical behavior has also been compared in terms of flow visualization. The streamlines of the flow have been captured at different α and ζ values. Figure 5.7 shows the streamlines at angle of attack $\alpha = 5°$, where the flow is chiefly attached to the airfoil. The positive effect of the cylinder rotation is not so apparent to the eye as it is quite small at such low angle of attack. However, it can be said that the experimental and CFD result closely match each other. It can be seen that the flow is attached to the airfoil in both cases, yet is starting to get slightly separated at the very end of the airfoil, near the trailing edge.
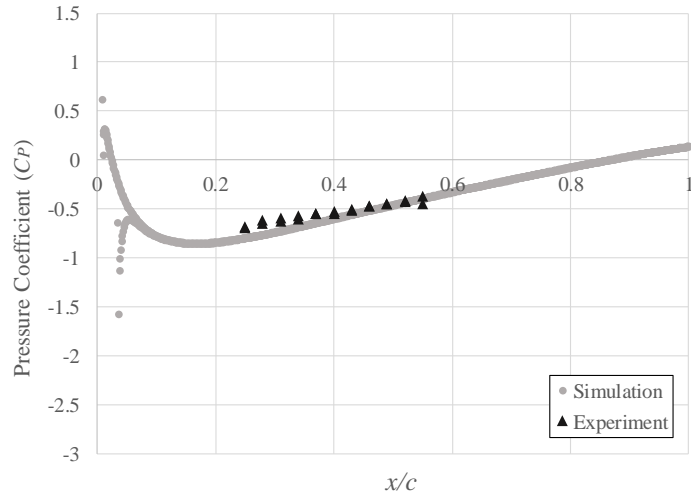
(a)
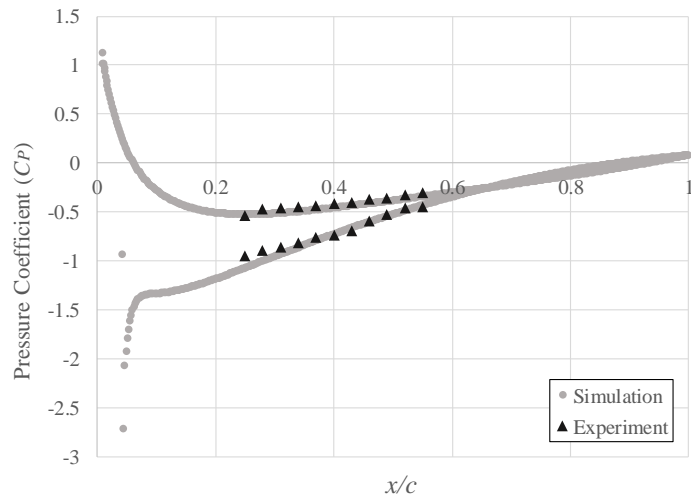
(b)
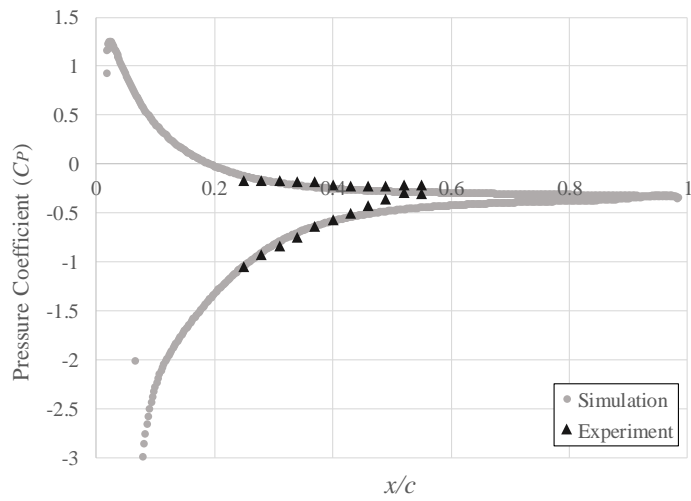
(c)

Figure 5.4: Simulation validation with experimental data. Plot of pressure coefficient vs. x/c at $\zeta = 0$ for (a) $\alpha = 0°$, (b) $\alpha = 5°$ and (c) $\alpha = 15°$.

46
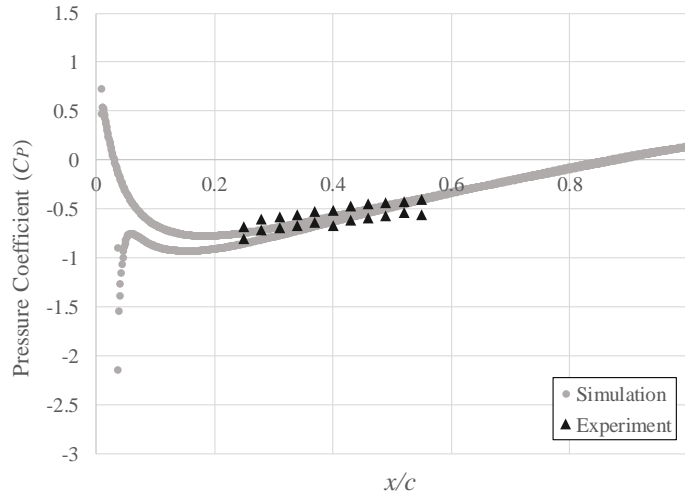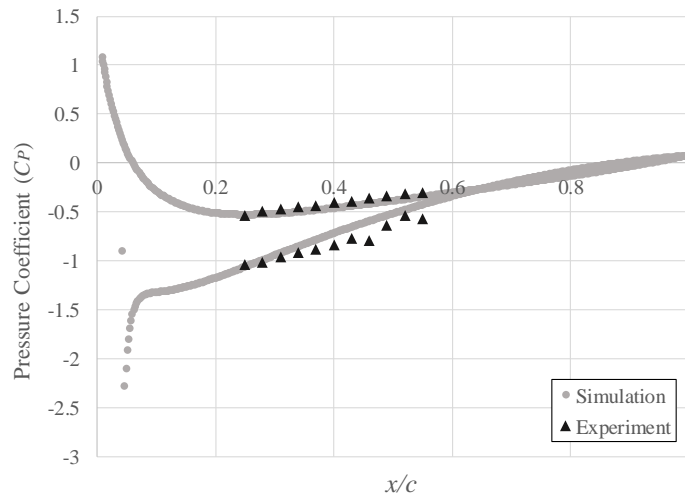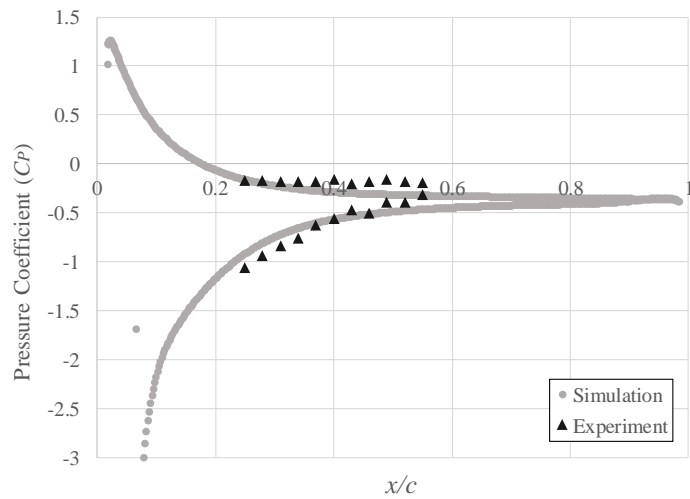
Figure 5.5: Simulation validation with experimental data. Plot of pressure coefficient vs. x/c at $\zeta = 1$ for (a) $\alpha = 0°$, (b) $\alpha = 5°$ and (c) $\alpha = 15°$
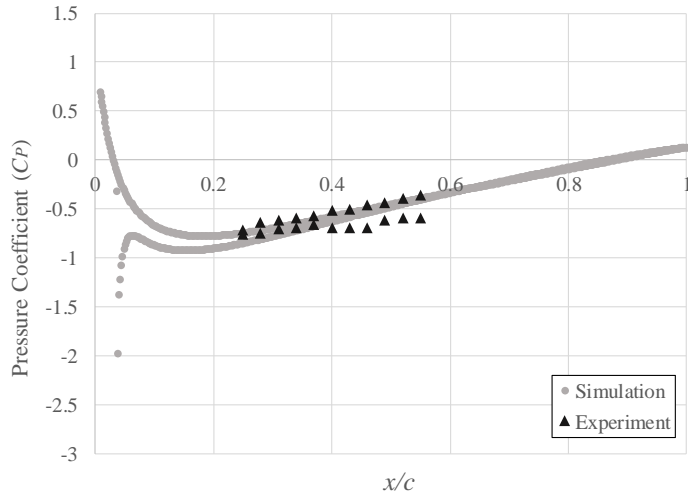
(a)
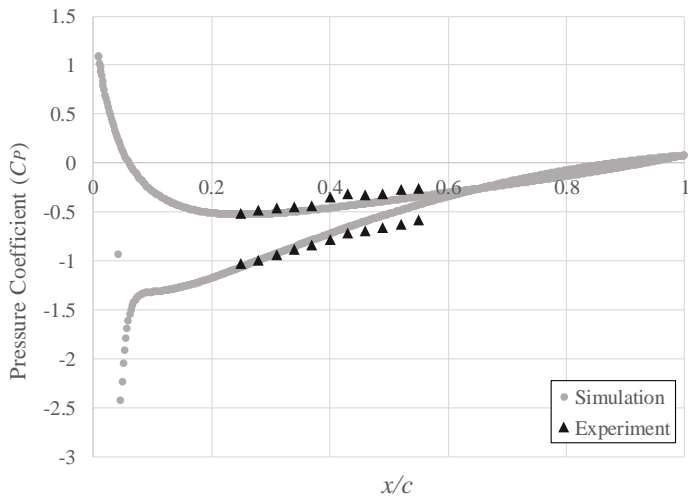
(b)
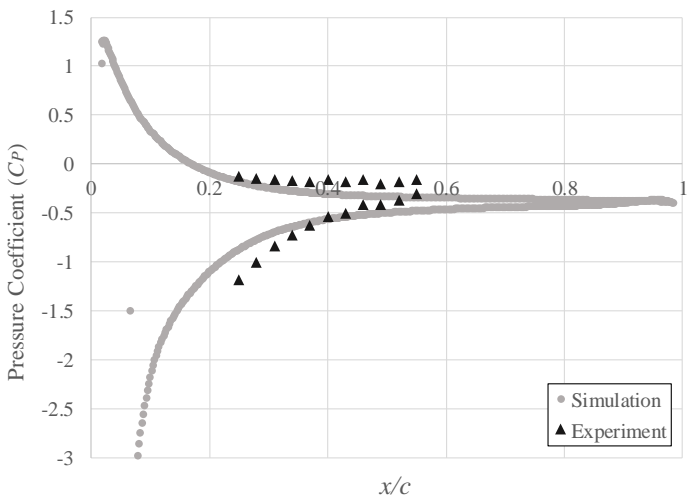
(c)

Figure 5.6: Simulation validation with experimental data. Plot of pressure coefficient vs. x/c at $\zeta = 2$ for (a) $\alpha = 0°$, (b) $\alpha = 5°$ and (c) $\alpha = 15°$.

(a)

(b)

(c)
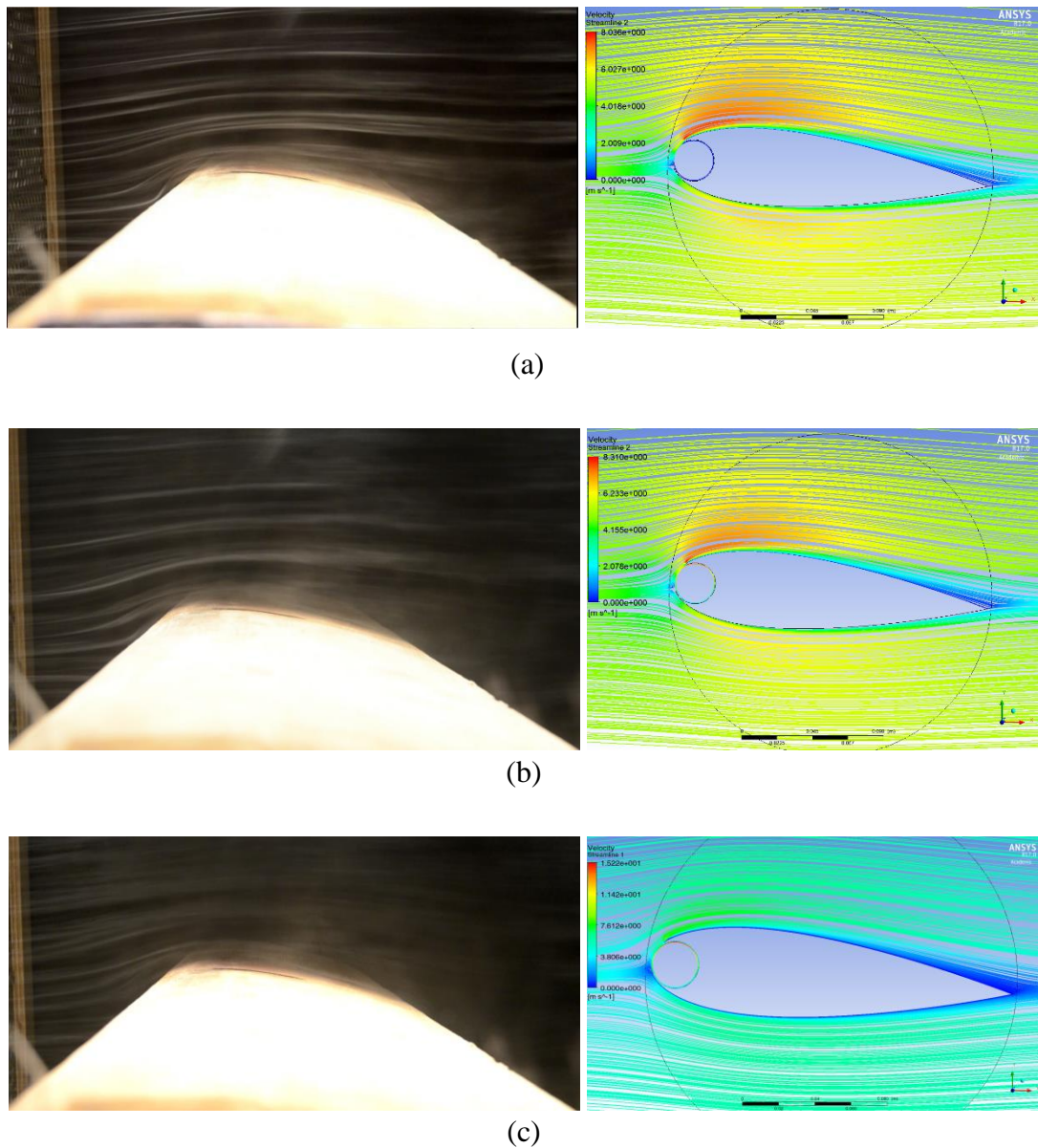
Figure 5.7: Flow visualization in experiment (left) and simulation (right) at $\alpha = 5°$ for (a) $\zeta = 0$, (b) $\zeta = 1$, and (c) $\zeta = 2$.

In a similar manner, Figure 5.8 shows visualization of the flow at angle of attack of $\alpha = 15°$, where separation predominantly starts to take place. At cylinder-to-freestream velocity ratio of $\zeta = 0$, it is clear and evident how the flow is separated very close to the leading edge, with eddies and reversed turbulent flow apparent at the separated portion. When the the rotation of the cylinder is implemented, however, the point of separation is slightly delayed, and the flow can be seen to remain attached for a longer segment, leading to a reduced separated turbulent region.
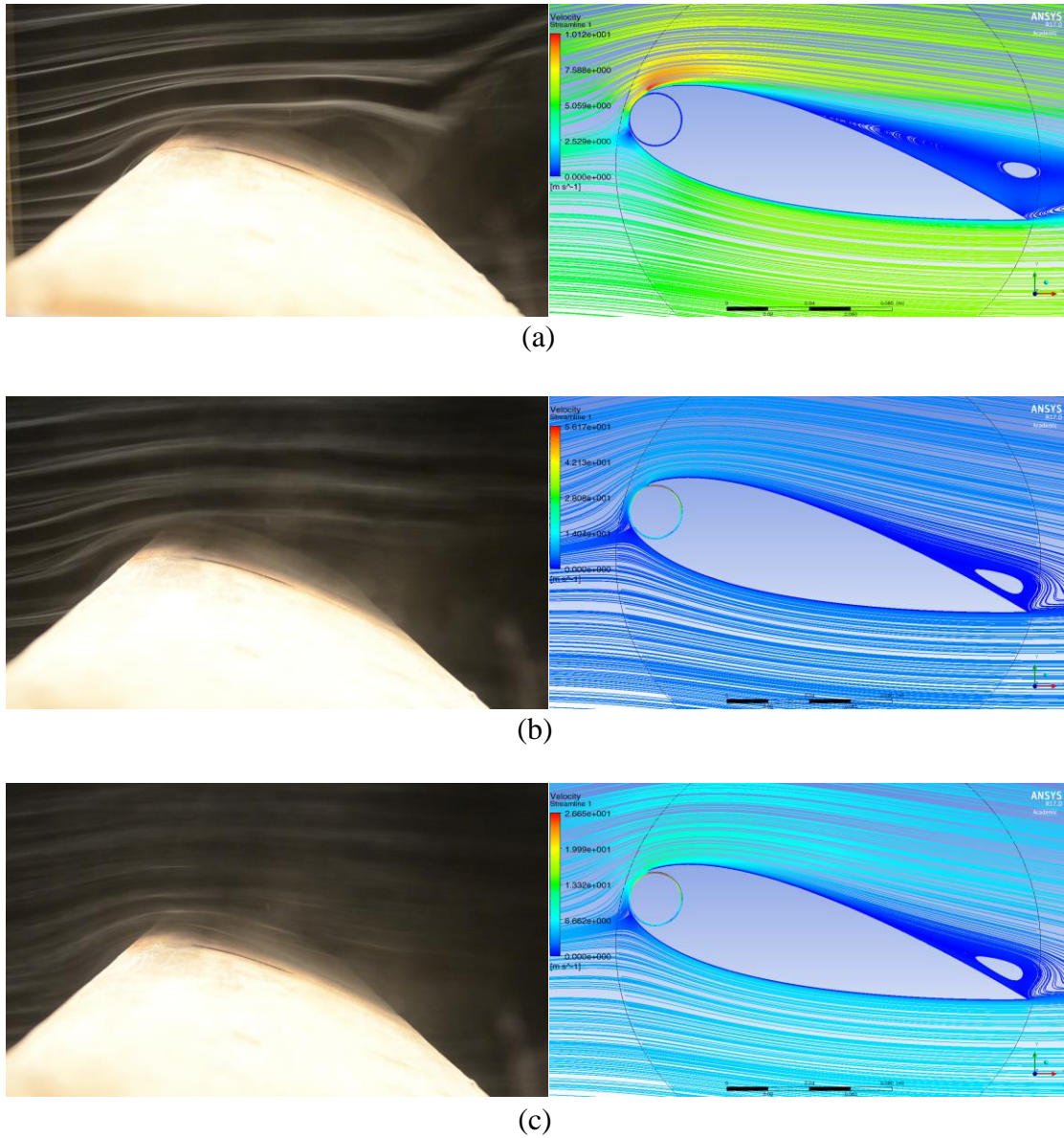
Figure 5.8: Flow visualization in experiment (left) and simulation (right) at $\alpha = 15°$ for (a) $\zeta = 0$, (b) $\zeta = 1$, and (c) $\zeta = 2$.

5.3. Variation of Cylinder-to-freestream Velocity Ratio

This section covers the results of variating the cylinder-to-freestream velocity ratio, ζ, to higher ends than those implemented in the experimental work. The tried ratios and their corresponding cylinder rotational speeds were shown earlier in Table 4.2.

5.3.1. Lift and drag coefficients. The lift coefficient is plotted against the angle of attack in Figure 5.9 for all attempted cylinder-to-freestream velocity ratios. The results show a substantial increase in lift coefficient as ζ is increased. At the base airfoil

case, i.e. when $\zeta = 0$, the maximum lift coefficient is obtained at $\alpha = 15°$, with a value of 0.98. However, with the cylinder rotation at $\zeta = 6$, the maximum lift coefficient is increased to a value of 1.45 at an angle of attack $\alpha = 25°$, which is about a 48% increase. The rotation of the cylinder has ultimately increased the stall angle of attack α_{stall} from 15-20° at $\zeta = 0$, to around 30° at $\zeta = 6$, which translates to around 71% increase.

Likewise, the drag coefficient has been plotted against the angle of attack in Figure 5.10 at the different cylinder-to-freestream velocity ratios. Similar to the experimental situation, the drag coefficient increased with increasing angle of attack and cylinder rotational speed, with the maximum value being at $\alpha = 30°$ in all cases. The maximum drag coefficient increased from 0.44 at $\zeta = 0$ to 0.65 at $\zeta = 6$.

Additionally, Figure 5.11 shows a plot of lift-to-drag ratio at the same range of angles of attack and velocity ratios. The maximum C_L/C_D, similar to its experimental counterpart, occurs at $\alpha = 5°$, and is improved with higher ζ, due to the improved lift coefficient and negligible difference of drag coefficient at this angle. It is good to note that at $\alpha = 0°$ and $\zeta = 0$, $C_L/C_D = 0$ due to the fact that the airfoil as zero lift at this incidence.
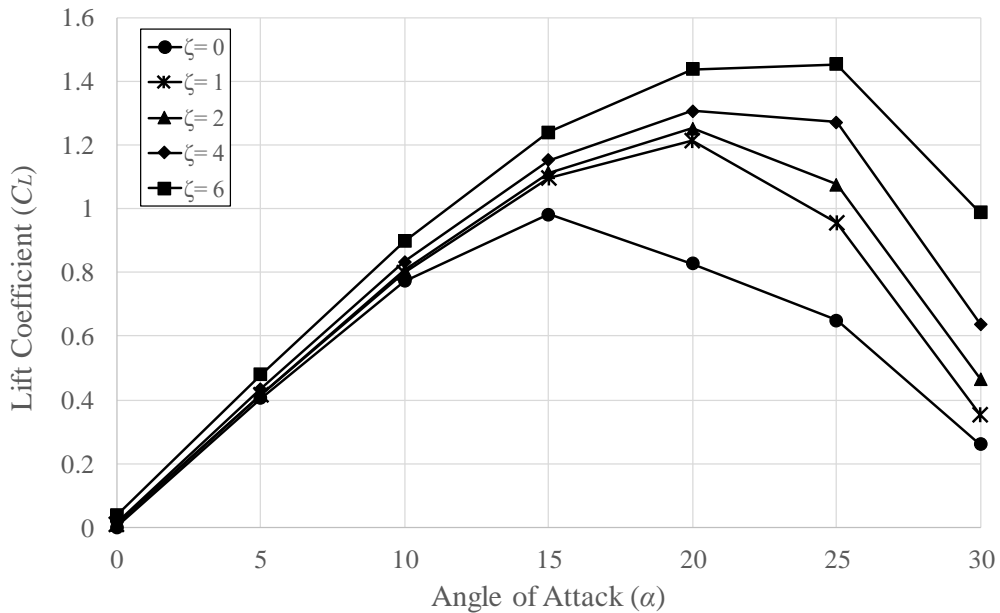
Figure 5.9: Lift coefficient (numerical) versus angle of attack at $\zeta = 0$, 1, 2, 4 and 6.
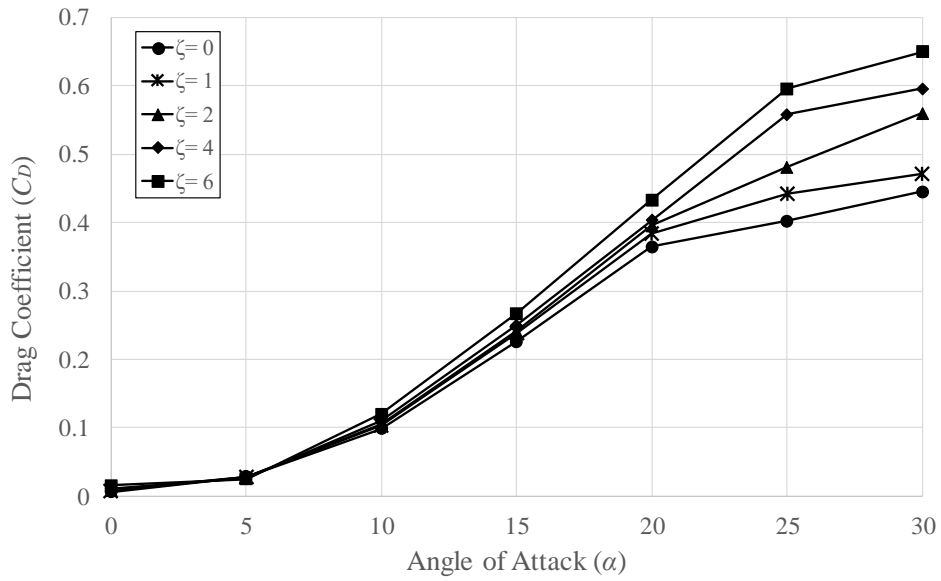
Figure 5.10: Drag coefficient (numerical) versus angle of attack at $\zeta = 0, 1, 2, 4$
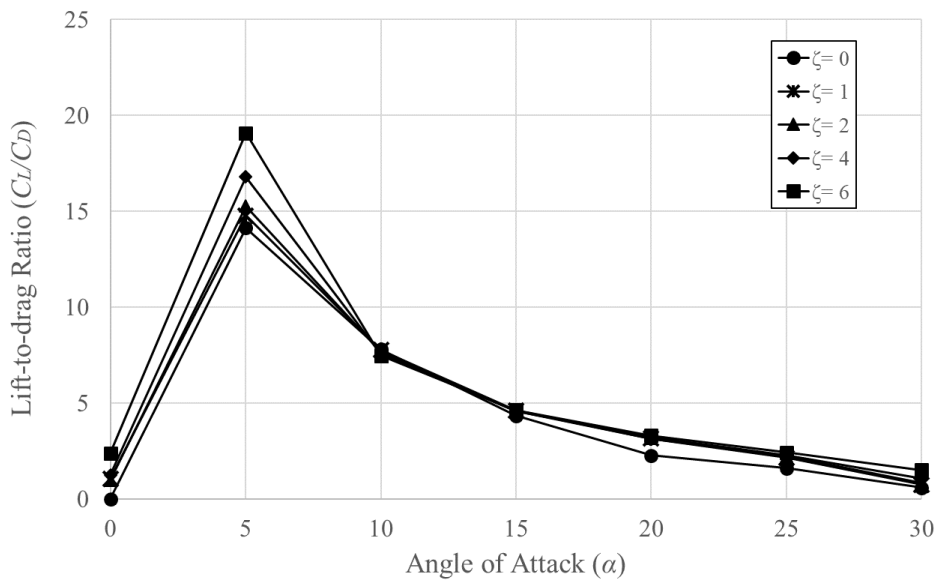
Figure 5.11: Lift-to-drag ratio (numerical) versus angle of attack at $\zeta = 0, 1, 2, 4$ and 6.

5.3.2. Flow visualization. Streamline shots of the flow have been taken at the numerous several cases of angles of attack and velocity ratios in order to closely observe the behavior of the flow with the change of the cylinder's rotational speed. The most notable situation is shown Figure 5.12, at $\alpha = 25°$ where the performance improvement is quite distinct. At $\zeta = 0$, the separation of the flow occurs quite close to the leading edge. However, as ζ is increased, the separation point is moved forward,

such that at $\zeta = 6$ the flow is almost completely attached to the upper surface of the airfoil, which explains the high value of lift coefficient discussed earlier.

(a)   (b)

(c)
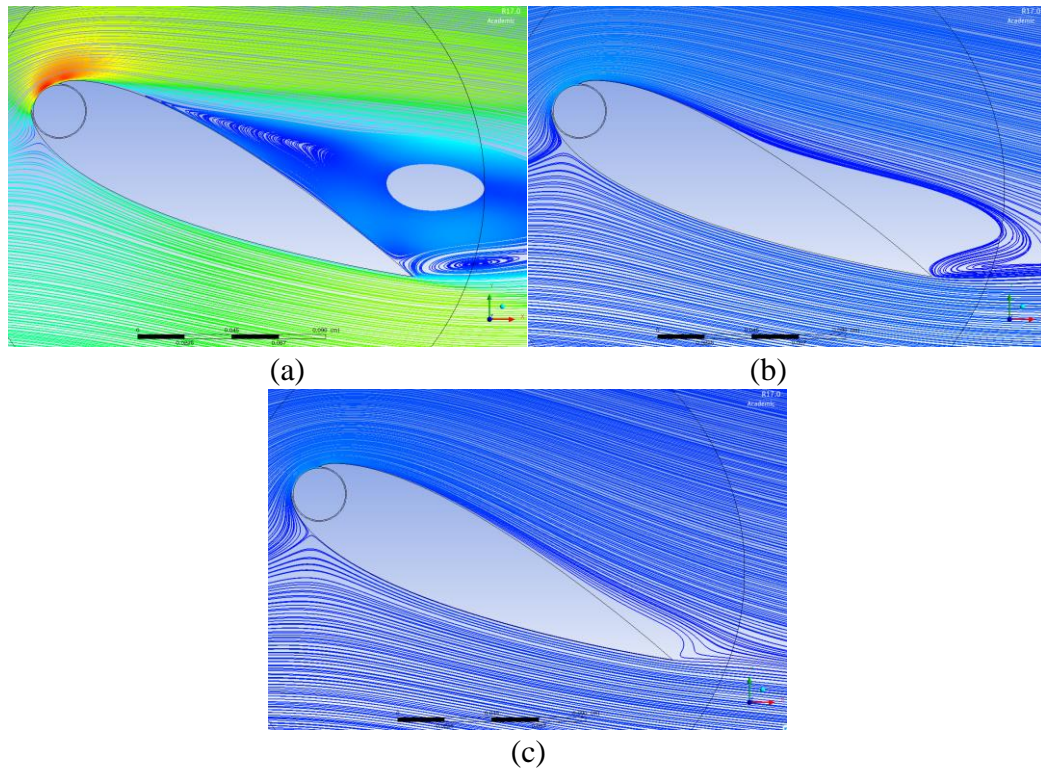
Figure 5.12: Flow visualization at $\alpha = 25°$ for (a) $\zeta = 0$, (b) $\zeta = 4$, and (c) $\zeta = 6$.

5.4.   Alternation of Cylinder Exposure

This section presents an overview of the results of the final study in this research. In this study, the exposure of the cylinder has been altered such that three different cases are obtained; 20% exposure, 30%, and 40%. The geometries of these different cases were shown earlier in Figure 4.9. The simulation has calculated at $\zeta = 4$ for $\alpha = 10°$ and 20°. Table 5.1 shows a summary of the aerodynamic coefficients at the three different exposures at $\alpha = 10°$, it can be noted that the lift coefficient increased by 6.6% as the exposure increased from 20% to 40%, however, that is accompanied by a 13.6% increase in drag. The lift to drag ratio has thus decreased by about 6.6% as well as a result of this change. Figure 5.13 shows the streamlines of the flow for this case. It can be noted that the stagnation point got slightly shifted downwards with the increase in exposure. The slight enhancement in boundary layer attachment can be seen at the portion of the airfoil's upper surface at 40% exposure, which results in a slightly increased lift coefficient.

Table 5.1: Lift coefficient, C_L, drag coefficient, C_D, and lift-to-drag ratio, C_L/C_D, at different cylinder exposures, at $\zeta = 4$ and $\alpha = 10°$

Exposure	C_L	C_D	C_L/C_D
20%	0.7439	0.1055	7.0511
30%	0.7650	0.1092	7.0055
40%	0.7933	0.1199	6.6163

(a)

(b)

(c)
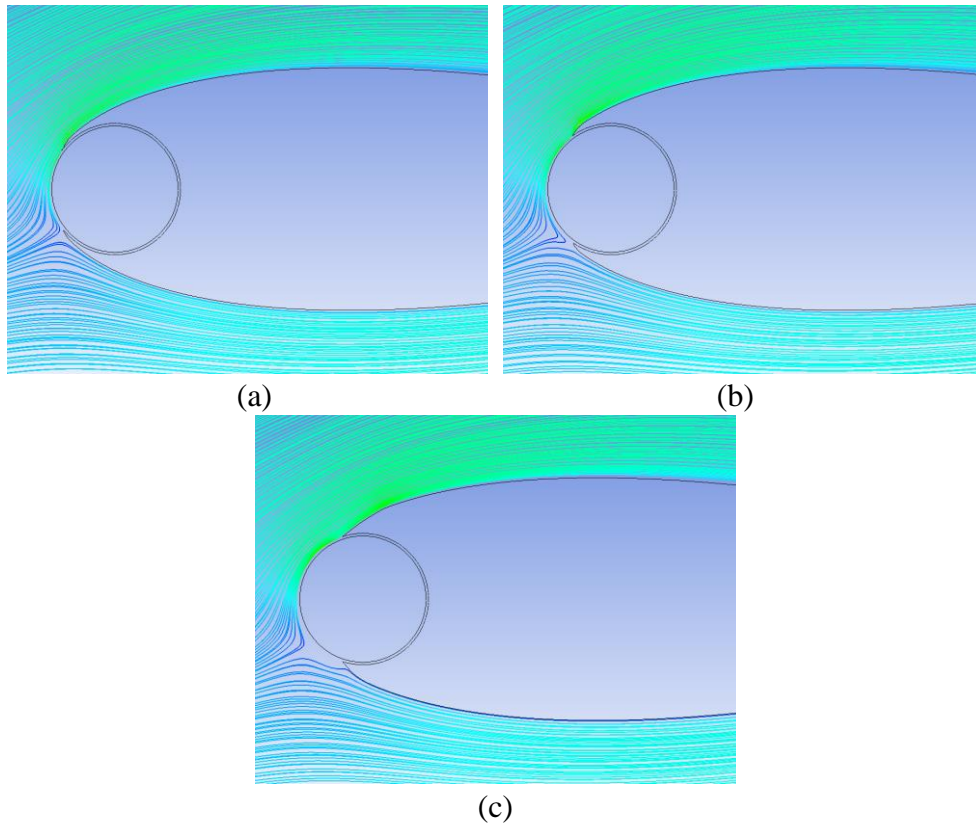
Figure 5.13: Flow visualization at $\zeta = 4$ and $\alpha = 10°$, for cylinder exposure of (a) 20% (b) 30%, and (c) 40%.

Similarly, Table 5.2 shows a summary of the aerodynamic parameters $\alpha = 20°$. In this case, the lift coefficient increased by about 19.6% with increased exposure from 20% to 40%, which is, yet again, accompanied by a 9.7% increase in drag. The lift-to-drag coefficient, however, has shown a notable increase of 9.1% this time.

Figure 5.14 shows the flow visualization for this second case. The stagnation point has moved further down towards the airfoil's lower surface due to the increased angle of attack. The effect of the increased exposure on the boundary layer separation

is clearer in this case. The separation point has moved slightly farther away at 40% exposure in comparison with the 20% exposure airfoil.

Table 5.2: Lift coefficient, C_L, drag coefficient, C_D, and lift-to-drag ratio, C_L/C_D, at different cylinder exposures, at $\zeta = 4$ and $\alpha = 20°$

| Exposure	C_L	C_D	C_L/C_D
20%	1.1618	0.1768	6.5713
30%	1.2895	0.1804	7.1480
40%	1.3895	0.1939	7.1661

(a)

(b)

(c)
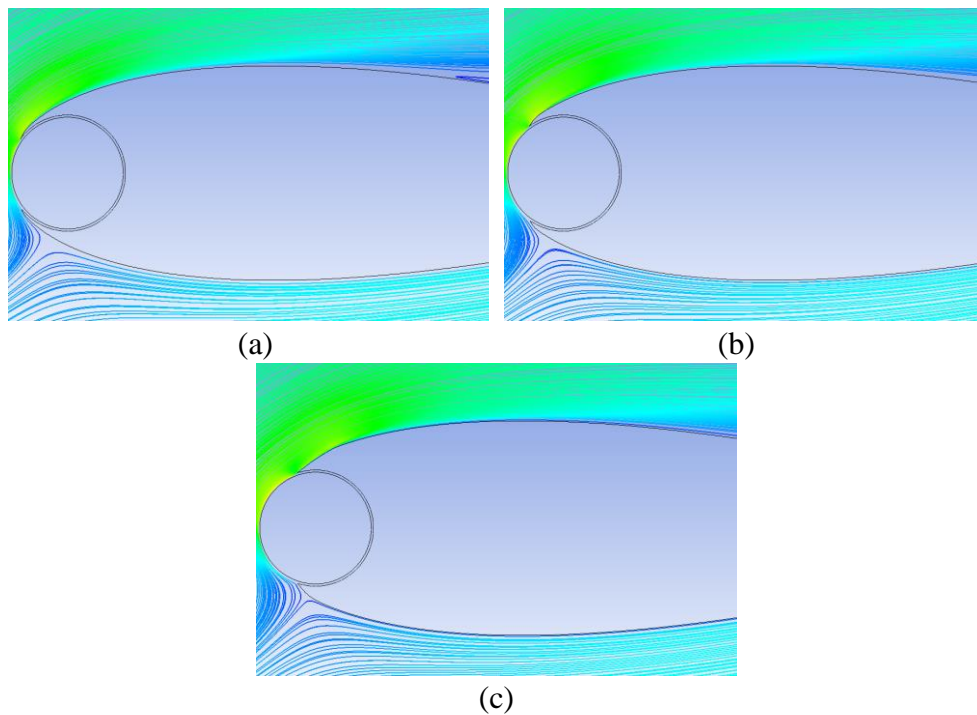
Figure 5.14: Flow visualization at $\zeta = 4$ and $\alpha = 20°$, for cylinder exposure of (a) 20% (b) 30%, and (c) 40%.

Figure 5.15 and Figure 5.16 show a summary of the comparison between the two studied angles of attack. The lift coefficient increased with increasing cylinder exposure at both cases, and so did the drag coefficient. The increase in lift coefficient, however, occurred in a higher rate at $\alpha = 20°$ than it did at $\alpha = 10°$. Figure 5.17 shows the overall lift-to-drag ratio for the two cases. The contrast between the two cases can be evidently observed. The lift-to-drag ratio decreased with increasing exposure at

angle of attack $\alpha = 10°$, while the opposite occurred at $\alpha = 20°$, where increasing the exposure had an enhancing effect on the lift-to-drag ratio.

Altering the exposure can thus be said to have a promising effect on enhancing the overall aerodynamic performance. As the general airfoil efficiency, in terms of lift-to-drag ratio, has shown a dissimilar outcome for the two cases discussed formerly, it is essential to conduct an optimization study such that the relatively best combination of the three variables $-\alpha$, ζ and exposure$-$ can be selected and operated.
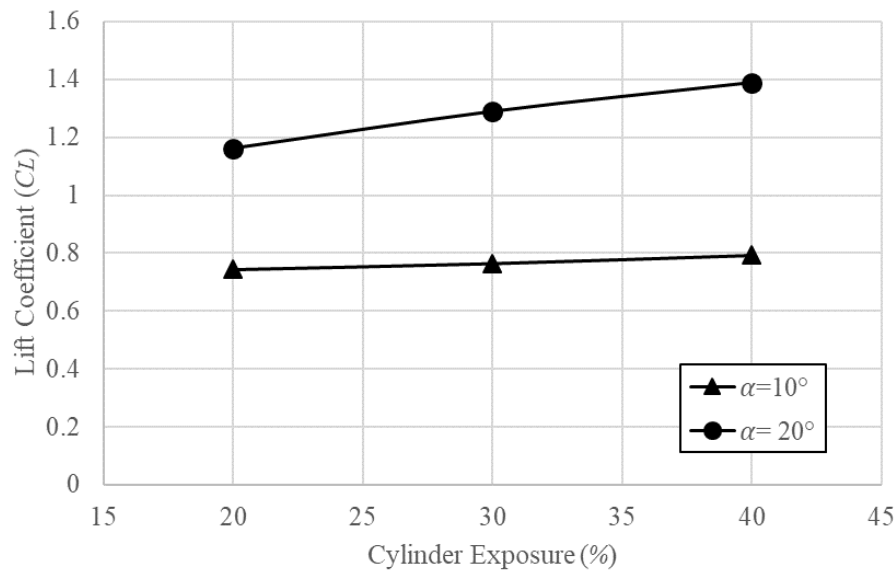

Figure 5.15: Lift coefficient versus cylinder exposure in percentage, at $\alpha = 10°$ and 20°, and $\zeta = 4$.
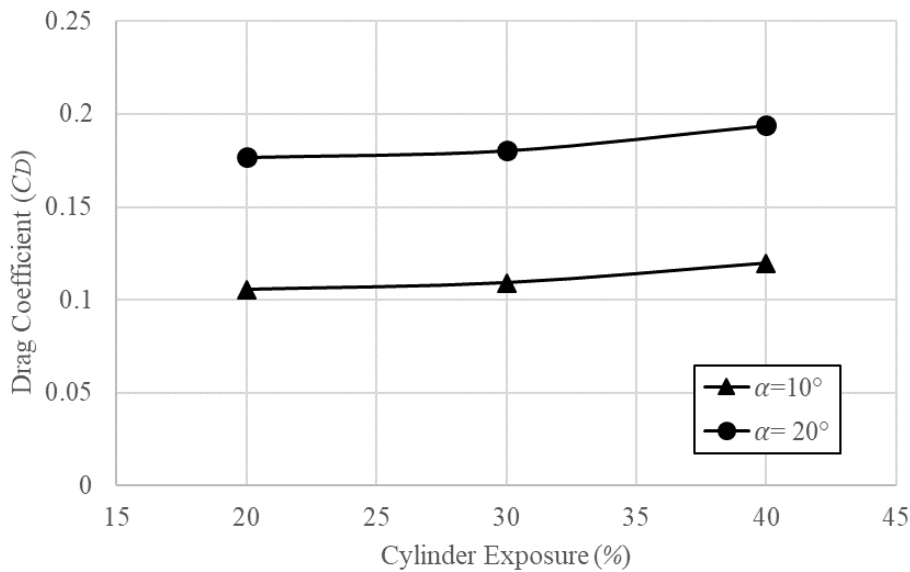
Figure 5.16: Drag coefficient versus cylinder exposure in percentage, at $\alpha = 10°$ and 20°, and $\zeta = 4$.
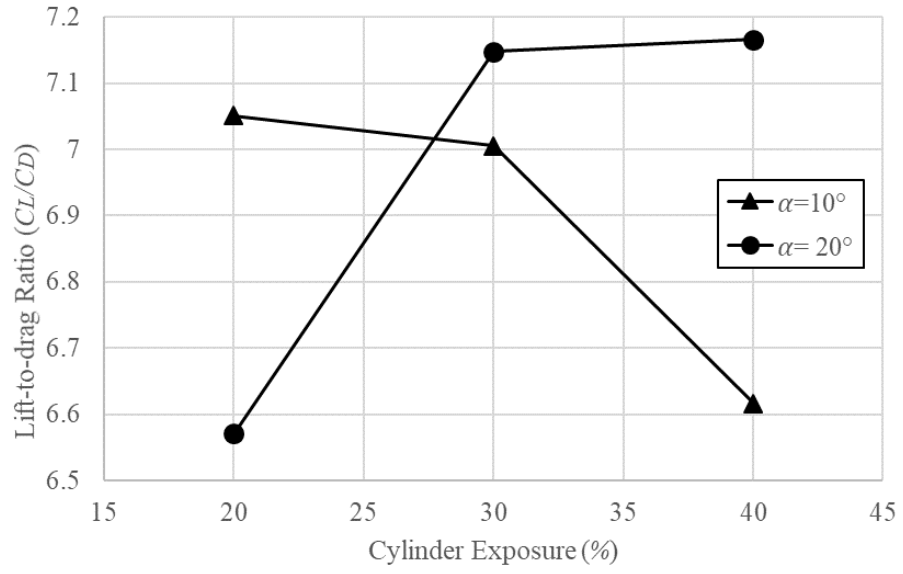
Figure 5.17: Lift-to-drag ratio versus cylinder exposure in percentage, at $\alpha = 10°$ and $20°$, and $\zeta = 4$.

Chapter 6. Conclusions and Future Work

This work presented an experimental and numerical study of a NACA0024 airfoil with a rotating cylinder embedded at its leading edge. The experimental work was conducted in a subsonic wind tunnel. Pressure data were collected, analyzed, and used as a validation point for the following numerical work. Experimental results showed a promising increase in lift as the cylinder-to-freestream velocity ratio was increased. Flow visualization shots have shown the pattern of the streamlines of the flow as they get affected by the rotation of the cylinder.

The numerical work was done through building a CFD model in ANSYS FLUENT software. Through comparison with the experimental data, the model was successfully validated. The numerical simulations were conducted using the SST k-ω turbulence model. After validation, the cylinder-to-freestream velocity ratio, ζ, was increased from 0 to 6, while monitoring its effect on the aerodynamic performance. Results showed an increase of the maximum lift coefficient between from 0.98 at $\zeta = 0$ to 1.45 at $\zeta = 6$, which translates to around 48% of increase. The corresponding stall angle of attack increased from $\alpha = 15°$ at $\zeta = 0$, to around $\alpha = 35°$ at $\zeta = 6$. This increase of lift parameter, however, is accompanied by an increase in drag, due to the decreased normal pressure on the airfoil's upper surface with the increased rotation of the cylinder.

Different exposures of the rotating cylinder were studied as well. Results showed a promising increase in the lift coefficient of 6.6% to 19.6% at $\alpha = 10°$ and 20°, respectively.

Future work may include an optimization study in order to find the combination of angle of attack, cylinder-to-freestream velocity ratio, and cylinder exposure that gives the best aerodynamic performance. In addition to including hybrid passive and active methods to improve lift to drag ratio, such as rotating cylinder with suction flow.

References

[1]   V. J. Modi, "Moving surface boundary-layer control: A review," *Journal of Fluids and Structure.*, vol. 11, pp. 627–663, Aug. 1997.

[2]   Y. A. Çengel and J. M. Cimbala, *Fluid mechanics: fundamentals and applications*, 1st ed. New York: McGraw-Hill, 2006.

[3]   M. A. Day, "The no-slip condition of fluid dynamics," *Erkenntnis*, vol. 33, pp. 285–296, Nov. 1990.

[4]   F. M. White, *Fluid mechanics*, 8th ed. New York.: McGraw-Hill, 2015.

[5]   M. Gad-el-Hak, *Flow control : passive, active, and reactive flow management*. Cambridge: Cambridge University Press, 2000.

[6]   H. Schlichting and K. Gersten, *Boundary-layer theory*, 9th ed. Berlin: Springer, 2016.

[7]   D. Crane, *Dictionary of Aeronautical Terms*, 5th ed. Newcastle: Aviation Supplies & Academics Inc., 2012.

[8]   G. M. Homsy, *Multi-media fluid mechanics*. Cambridge: Cambridge University Press, 2000.

[9]   D. C. Hazen. "Film Notes for Boundary-Layer Control." *National Committee for Fluid Mechanics Films* (1968), No. 21614 pp. 1-8.

[10]   A. Ulrich, "Theoretical investigation of drag reduction in maintaining the laminar boundary layer by suction." *National Advisory Commitee for Aeronautics* (Jun., 1947), No. 1121 pp. 32-55.

[11]   J. D. McLean and H. J. Herring, "Use of multiple discrete wall jets for delaying boundary layer separation." *National Aeronautics and Space Administration*, 1974, pp. 12-32.

[12]   S. E. James, A. Suryan, J. J. Sebastian, A. Mohan, and H. D. Kim, "Comparative study of boundary layer control around an ordinary airfoil and a high lift airfoil with secondary blowing," *Computers & Fluids*, vol. 164, pp. 50–63, Mar. 2018.

[13]   F. Mokhtarian, "Fluid Dynamics of Airfoils with Moving Surface Boundary-Layer Control," Ph.D. Thesis, The University of British Columbia, Canada, 1988.

[14]   A. Favre, *Contribution à l'étude expérimentale des mouvements hydrodynamiques à deux dimensions*. Paris: E. Blondel La Rougery, 1938.

[15]   J. Seifert, "A review of the Magnus effect in aeronautics," *Progress in Aerospace Sciences*, vol. 55, pp. 17–45, Nov. 2012.

[16]   E. B. Wolff, "Preliminary Investigation of the Effect of a Rotating Cylinder in a Wing," *National Advisory Committee for Aeronautics*, 1925, pp. 7-14.

[17]   E. B. Wolff and C. Koning, "Tests for determining the effect of a rotating cylinder fitted into the leading edge of an airplane wing," presented at the International Congress of Aerial Navigation, Amsterdam, Netherlands, 1926.

[18]   J. S. Tennant, W. S. Johnson, and A. Krothapalli, "Rotating cylinder for circulation control on an airfoil," *J. Hydronautics*, vol. 10, pp. 102–105, Jul. 1976.

[19]   J. S. Tennant, W. S. Johnson, and D. D. Keaton, "Boundary-layer flows from fixed to moving surfaces including gap effects," *J. Hydronautics*, vol. 12, pp. 81–84, Apr. 1978.

[20]   A. Z. Al-Garni, A. M. Al-Garni, S. A. Ahmed, and A. Z. Sahin, "Flow Control for an Airfoil with Leading-Edge Rotation: An Experimental Study," *Journal of Aircraft*, vol. 37, pp. 617–622, Jul. 2000.

[21]   V. J. Modi, S. R. Munshi, G. Bandyopadhyay, and T. Yokomizo, "High-performance airfoil with moving surface boundary-layer control," *Journal of Aircraft*, vol. 35, pp. 544–553, Jul. 1998.

[22]   R. Sahu and B. S. V. Patnaik, "CFD simulation of momentum injection control past a streamlined body," *International Journal of Numerical Methods for Heat and Fluid Flow*, vol. 21, pp. 980–1001, Nov. 2011.

[23]   D. Greenblatt and I. Wygnanski, "Effect of Leading-Edge Curvature on Airfoil Separation Control," *Journal of Aircraft*, vol. 40, pp. 473–481, May 2003.

[24]   Y. Zhuang, X. Sun, D. Huang, and G. Wu, "Numerical study on aerodynamic performances of the wind turbine rotor with leading-edge rotation," *Journal of Renewable and Sustainable Energy*, vol. 4, Nov. 2012.

[25]   L. N. Sankar, R. Marpu, and Y. Yu, "On the Use of Rotating Leading Edge Devices in Wind Turbine Blades for Increased Power Production and Vibration Reduction," presented at the 2013 World Congress on Advances in Nano, Biomechanics, Robotics, and Energy Research, Seoul, Korea 2013.

[26]   A. Nazari, "Control of Flow Past an Airfoil Section Using Rotating Cylinders," M.Sc. Thesis, American University of Sharjah, United Arab Emirates, 2015.

[27]   A. J. Smits and T. T. Lim, *Flow Visualization: Techniques and Examples*. London: Imperial College Press, 2014.

[28]   J. F. Manwell, J. G. McGowan, and A. L. Rogers, *Wind energy explained: theory, design and application*, 2nd ed. Wiltshire: Wiley, 2010.

[29]   J. D. Anderson, *Fundamentals of Aerodynamics*, 6th ed. Boston: McGraw-Hill, 2017.

[30]   B. R. Munson, T. H. Okiishi, A. P. Rothmayer, and W. W. Huebsch, *Fundamentals of fluid mechanics*, 6th ed. Jefferson City: John Wiley & Sons Inc., 2012.

[31]   J. Moran, *An Introduction to Theoretical and Computational Aerodynamics*. New York: Dover Publications, 2003.

[32]   K. Yousefi and A. Razeghi, "Determination of the Critical Reynolds Number for Flow over Symmetric NACA Airfoils," presented at 2018 AIAA Aerospace Sciences Meeting, Kissimmee, Florida, United States, 2018.

[33] S. M. Salim and S. Cheah, "Wall Y+ strategy for dealing with wall-bounded turbulent flows," in *Proceedings of the international multiconference of engineers and computer scientists*, 2009, vol. 2, pp. 2165–2170.

[34] ANSYS, Inc. Training Lecture, Topic: "Introduction to ANSYS FLUENT Lecture 7: Turbulence Modeling.", Feb. 28, 2014.

[35] M. Jousef, "What is y+ (yplus)?," Internet: www.simscale.com/forum/t/what-is-y-yplus/82394, May 2018 [Mar. 14, 2019].

[36] A. Al-Abdullah, M. I. Qureshi, and M. Hamdan, "Appropriate Turbulence Model for Simulating Airfoil with Rotating Leading-edge," presented at the 5th Graduate Students Research Conference, Abu Dhabi, United Arab Emirates, 2019.

[37] ANSYS, Inc. "ANSYS Academic Research Mechanical, Release 17.0, Help System, Fluent, Modeling Turbulence."

[38] D. C. Eleni, T. I. Athanasios, and M. P. Dionissios, "Evaluation of the turbulence models for the simulation of the flow over a National Advisory Committee for Aeronautics (NACA) 0012 airfoil," *Journal of Mechanical Engineering Research*, vol. 4, pp. 100–111, Mar. 2012.

[39] S. B. Pope, *Turbulent flows*. Cambridge: Cambridge University Press, 2000.

[40] F. Menter, "Zonal two equation kw turbulence models for aerodynamic flows," presented at the 23rd Fluid Dynamics, Plasmadynamics, And Lasers Conference, Orlando, Florida, United States, 1993.

[41] F. R. Menter, "Two-equation eddy-viscosity turbulence models for engineering applications," *AIAA J.*, vol. 32, pp. 1598–1605, Aug. 1994.

[42] A. Al-abdullah and M. I. Qureshi, "Experimental and Numerical Setup for An Airfoil with Rotating Leading-Edge Cylinder Study," presented at the 8th International Conference on Modeling, Simulation & Applied Optimization, Amwaj Islands, Bahrain, 2019.

[43] A. Alhourani, D. Madurawala, M. Amer, M. Omran, and S. Hassan, "Performance Optimization of a NACA Wing Section using a Leading Edge Rotating Cylinder," B.Sc. senior design project, American University of Sharjah, United Arab Emirates, 2018.

Vita

Anfal Al-Abdullah was born in 1993 in Iraq. She received her primary and secondary education in Al-Shola Private School, Sharjah, UAE. She continued her post-secondary education and obtained a B.Sc. degree in Sustainable and Renewable Energy Engineering from the University of Sharjah in 2015.

In September 2016, she joined the Mechanical Engineering master's program in the American University of Sharjah as a graduate teaching assistant. During her master's study, she co-authored one journal paper in addition to two conference papers, which were presented in international conferences.